

JRC-27-2003

CHARACTERIZATION OF SEISMOACOUSTIC
PROPERTIES OF MARINE SEDIMENTS

Jacques R. Chamuel
September 2003



Sonoquest

Advanced Ultrasonics Research

POST OFFICE BOX 81153 • WELLESLEY HILLS, MASSACHUSETTS 02181-0001, USA

National Technical Information Service
Accession Report No. AD-A_____

JRC-27-2003

CHARACTERIZATION OF SEISMOACOUSTIC
PROPERTIES OF MARINE SEDIMENTS

Jacques R. Chamuel
September 2003

DISTRIBUTION STATEMENT A
Approved for Public Release
Distribution Unlimited

20031104 005

Sonoquest Advanced Ultrasonics Research
P. O. Box 81153, Wellesley Hills, Massachusetts 02481-0001, USA

© Sonoquest Advanced Ultrasonics Research, 2003
*The U.S. Government is authorized to reproduce and sell this copyrighted
work. Permission for further reproduction must be obtained from the
copyright owner.*

This report is available from National Technical Information Service, U. S. Dept. of Commerce, 5285 Port
Royal Road, Springfield, VA 22161 Tel. (703) 487-4650

REPORT DOCUMENTATION PAGE

Form Approved
OMB No. 0704-0188

Public reporting burden for this collection of information is estimated to average 1 hour per response, including the time for reviewing instructions, searching existing data sources, gathering and maintaining the data needed, and completing and reviewing the collection of information. Send comments regarding this burden estimate or any other aspect of this collection of information, including suggestions for reducing this burden, to Washington Headquarters Services, Directorate for Information Operations and Reports, 1215 Jefferson Davis Highway, Suite 1204, Arlington, VA 22202-4302, and to the Office of Management and Budget, Paperwork Reduction Project (0704-0188), Washington, DC 20503.

1. AGENCY USE ONLY (Leave blank)			2. REPORT DATE September 2003	3. REPORT TYPE AND DATES COVERED Final Report July 2002-September 2003
4. TITLE AND SUBTITLE CHARACTERIZATION OF SEISMOACOUSTIC PROPERTIES OF MARINE SEDIMENTS			5. FUNDING NUMBERS C-N00014-02-C-0377	
6. AUTHOR(S) Jacques R. Chamuel				
7. PERFORMING ORGANIZATION NAME(S) AND ADDRESS(ES) Sonoquest Advanced Ultrasonics Research P. O. Box 81153 Wellesley Hills, MA 02481-0001			8. PERFORMING ORGANIZATION REPORT NUMBER JRC-27-2003	
9. SPONSORING/MONITORING AGENCY NAME(S) AND ADDRESS(ES) Office of Naval Research, Code 3210A 800 N. Quincy St. Arlington, VA 22217-5660			10. SPONSORING/MONITORING AGENCY REPORT NUMBER	
11. SUPPLEMENTARY NOTES ONR POC-Dr. Ellen Livingston (Dr. Jeffrey Simmen (703)-696-4204)				
12a. DISTRIBUTION/AVAILABILITY STATEMENT Approved for Public Release			12b. DISTRIBUTION CODE Distribution Unlimited	
13. ABSTRACT (Maximum 200 words) Experimental findings are presented on fundamental seismoacoustic characteristics of unconsolidated sediments not explained by existing theories. Precision measurements of the compressional velocity "C _p " in coarse water-saturated sand revealed that C _p decreased by 14% as frequency increased from 80 to 880 kHz, while the Biot theory predicted an increase of < 1 %. Measured dispersion in saturated fine sand and glass beads had a similar trend. Data from Kings Bay Experiment by Chotiros (1995) were replotted indicating that C _p decreased by 6% as frequency increased from 5 to 60 kHz. C _p in drained sand and glass beads remained near the saturated value 1750m/s in contrast with the 85% decrease predicted by the low-frequency Biot-Gassman theory. Time-dependent stiffening was detected in drained sediments. Visualization of capillary mechanisms using seawater and glass microplates provided physical insight into grain to grain coupling and time-dependent properties. Unique features were observed on crystallization in confined geometry, solid-like behavior of confined seawater, cavitation, and shear coupling. Capillary experiments on gassy sediments showed that when air was injected in water-saturated sand, oblique 45° fracture cracks formed in the sand as it became locally unsaturated. The cracks were perpendicular to each other originating from the air source location.				
14. SUBJECT TERMS			15. NUMBER OF PAGES 43	
			16. PRICE CODE	
17. SECURITY CLASSIFICATION OF REPORT Unclassified	18. SECURITY CLASSIFICATION OF THIS PAGE Unclassified	19. SECURITY CLASSIFICATION OF ABSTRACT Unclassified	20. LIMITATION OF ABSTRACT UL	

ABSTRACT

Experimental findings are presented on fundamental seismoacoustic characteristics of unconsolidated sediments not explained by existing theories. Precision measurements of the compressional velocity "C_p" in coarse water-saturated sand revealed that C_p *decreased* by 14% as frequency increased from 80 to 880 kHz, while the Biot theory predicted an *increase* of < 1 %. Measured dispersion in saturated fine sand and glass beads had a similar trend. Data from Kings Bay Experiment by Chotiros (1995) were replotted indicating that C_p decreased by 6% as frequency increased from 5 to 60 kHz. C_p in drained sand and glass beads remained near the saturated value (1750 m/s) in contrast with the 85% decrease predicted by the low-frequency Biot-Gassman theory. Time-dependent stiffening was detected in drained sediments. Visualization of capillary mechanisms using seawater and glass microplates provided physical insight into grain to grain coupling and time-dependent properties. Unique features were observed on crystallization in confined geometry, solid-like behavior of confined seawater, cavitation, and shear coupling. Capillary experiments on gassy sediments showed that when air was injected in *water-saturated* sand, oblique 45° fracture cracks formed in the sand as it became locally unsaturated. The cracks were perpendicular to each other originating from the air source location.

ACKNOWLEDGEMENTS

The research presented in this report was sponsored by the U.S. Office of Naval Research Code 321OA under Contract No. N00014-02-C-0377. The author is indebted to Dr. Jeffrey Simmen for making this research possible. The author would like to thank Prof. Michael J. Buckingham for providing the black spherical glass beads, and Prof. Nicholas P. Chotiros for suggesting the existence of the paper by Guillon et al. (1998).

TABLE OF CONTENTS

	Page
ABSTRACT -----	2
ACKNOWLEDGEMENTS -----	3
TABLE OF CONTENTS -----	4
I. INTRODUCTION -----	5
II. DISPERSION OF HIGH-FREQUENCY COMPRESSIONAL WAVES IN SATURATED SEDIMENTS -----	7
III. DRAINED SEDIMENT -----	16
IV. CAPILLARY CAVITATION AND CRYSTALLIZATION -----	19
- Visualization Studies and Background on Related Issues -----	19
- Ultrasonic Shear Wave Coupling -----	31
V. CAPILLARY PHENOMENA IN GASSY SEDIMENTS -----	35
VI. CONCLUSION-----	39
VII. REFERENCES -----	40

I. INTRODUCTION

Reliable detection and imaging of buried objects in the seabed requires fundamental understanding of high-frequency seismoacoustic phenomena under various realistic conditions. Mechanisms responsible for observed high attenuation and subcritical penetration of high-frequency acoustic waves in the ocean bottom are not yet understood [1-23]. Different researchers treated the seabed as a fluid with no rigidity, as an elastic solid, or as a viscous elastic material. Sand is an unstable medium and can change from a liquefied state to a stiff matrix. Subcritical penetration of incident underwater acoustic waves depends on refraction and knowing the frequency-dependence of the compressional and shear wave velocities. Hundreds of papers have been published on the Biot theory for saturated porous materials [1, 3-9, 11, 14, 22-31]. Two types of compressional waves are known to exist according to the Biot theory, however the Biot slow wave has not yet been observed in water-saturated sand. Hickey and Sabatier [7] characterized the dispersion of a slow compressional wave in air-filled sand. Boyle and Chotiros [4] observed an anomalous slow compressional wave (1200 m/s) in water-saturated sand. The sand frame bulk modulus given by Chotiros [22] was much greater than the known value, and the sand grains bulk modulus was five times smaller than the typical magnitude [1]. The Biot-Stoll poro-elastic model [30] depends on a large number of parameters to predict the seismoacoustic response of a particular sediment [1,22]. Chotiros [5] developed an extended Biot model and obtained an inversion for Biot parameters in saturated sand. Briggs [8] obtained empirical relationships relating sediment sound speed, attenuation, and density to sediment properties and composition. Yamamoto [28] related attenuation to permeability in sandy bottom. Turgut [29] used the Kramers-Kronig relations to characterize attenuation and dispersion. Williams [6] introduced an "effective density" fluid model. Mu and Badiey [14] examined the effect of the parameter uncertainty on the predicted response. Williams et al. [9] indicated that the Biot theory models fairly well the dispersion, however, the attenuation deviates. in the frequency range 125Hz to 400 KHz. Buckingham [12, 20, 32] developed a linear theory for saturated unconsolidated sediments possessing no skeletal frame with weak logarithmic dispersion due to attenuation consistent with Kramers-Kronig relationships. Gilbert and Panchenko [33] derived viscoelastic equations similar to Buckingham's using frictional energy dissipation with a microscopic length scale.

In Section II, precision laboratory measurements are presented on the dispersion of compressional waves C_p in coarse water-saturated sand revealing that C_p decreased by 14% as the frequency increased from 80 kHz to 880 kHz. According to the Biot-Stoll theory, the compressional wave velocity should increase by less than 1% as frequency is increased from 50 kHz to 1Mhz . The author observed a similar dispersion trend in saturated fine sand and glass beads. Following the distribution of a brief communication on the newly observed dispersion results [34], Prof. N. Chotiros suggested a paper by Guillon et al. [35] having also observed similar dispersion in water-saturated sand. The author is grateful to Prof. Chotiros for revealing Guillon's paper. Section I includes replotted low-frequency field data from Kings Bay Experiment by Chotiros [22] indicating that C_p decreased by about 6% as the frequency increased from 5 to 60 kHz.

In Section III, some experimental results on drained sediments are discussed. The compressional wave velocity in drained sand and glass beads remained near the saturated value (>1750 m/s) in contrast with the 85% decrease predicted by the low-frequency Biot-Gassman theory [87]. Time-dependent stiffening was observed in the drained glass beads. Two types of spherical glass beads are mentioned in the report: a) black glass beads (~250 μm) provided by Prof. M. J. Buckingham, and clear glass beads (430-600 μm) obtained from Potters Industries (P-0230).

The Buckingham theory for unconsolidated sediments [12, 20, 32], assumes the elastic rigidity modulus of the sediment to be zero, however, a "dissipative rigidity" is introduced that depends on frictional shear rigidity. The author was interested in understanding the basic problem of grain to grain coupling due to hidden adhesion mechanisms in the "absence" of roughness. Section IV presents a series of photographs visualizing fundamental capillary mechanisms using seawater and glass microplates. The purpose of the studies was to develop better understanding of grain to grain contact coupling and time-dependent properties of marine sediments under various conditions including the cavitation and rupture of the thin water film between the grains. The qualitative results identified unique properties of salt crystallization in confined geometry, air entrainment, trapping of water layer, solid-like behavior of confined water layer, rupture and cavitation of the trapped water film, dendritic type crystallization, formation of seals, shear wave coupling, stiffening with aging, and loading hysteresis.

Section V describes experimental findings on capillary phenomena in gassy sediments. The results demonstrated that when air was injected in *water-saturated* sand, oblique 45° angled fracture cracks developed in the sand. The formed cracks were perpendicular to each other originating from the air source location. The sand became locally transformed by the added stiffness, the elongated cracks, and the capillary forces clearly indicated the limitation of the theoretical sediment bubble model by Anderson and Hampton [36] representing the sediment as a fluid with no rigidity. Johnson, Gardiner, and Boudreau [37, 38] observed flattened vertical disc-shaped methane bubbles in marine sediments caused by fracture following linear elastic fracture mechanisms theory.

The goal of the research is to achieve better physical understanding of fundamental littoral seismoacoustic phenomena on the interaction of underwater acoustic waves with marine sediments leading to accurate acoustic modeling of littoral surficial layer and reliable seismoacoustic detection of buried objects.

II. DISPERSION OF HIGH-FREQUENCY COMPRESSIONAL WAVES IN SATURATED SEDIMENTS

In high frequency acoustics, it is important to know the seismoacoustic properties of the top layer of the seafloor (few centimeters) controlling the interaction and conversion on underwater acoustic waves. Surprising results obtained under the previous ONR contracts on the effect of water content on the compressional velocity C_p in sand raised some questions about the established dispersion trend predicted by the Biot theory (C_p increases as frequency increases) in saturated sand [39-41]. A series of precision laboratory measurements were conducted under controlled conditions to examine closely the frequency dependence of the compressional velocity in saturated sediments.

Measurements were carried out on fine sand, coarse sand, and glass beads in distilled water after removing any trapped air bubbles. Initially, the source was excited with a single broadband pulse to identify and eliminate undesired reflections that can interfere with the dispersion measurements. Fig. 1 shows the received dispersed waveform when a single pulse was propagated in fine saturated sand (Narragansett Beach, RI) recorded at two different ranges $X = 8$ cm and $X = 19.085$ cm. The width of the dispersed wavetrain increased as X was increased. The compressional wave was attenuated in the wet sand. The vertical amplification setting was 2 V/div. for the left trace, and 200 mV/div. for the right trace (Fig. 1). The oscilloscope trigger position was 42 μ s and 108 μ s, respectively.

Fig. 2 shows compressional waveforms in saturated black glass beads captured at three distances ($X = 2, 4$, and 6 cm). Waveforms from saturated fine sand, medium sand, and coarse sand (750-1500 μ m) are compared in Fig. 3 measured at $X = 8$ cm. Compaction increased C_p as demonstrated in Fig. 4, by comparing the arrival time of liquefied and compacted black glass beads ($X = 18.639$ cm). Compaction decreased the arrival time by about 1.66%.

The dispersion characteristic in saturated sediments was practically independent of the wave path direction (horizontal or vertical), and independent of the transducers depth (between 3-10 cm) as shown in Fig. 5 and Fig. 6, respectively. The water depth had no effect on the dispersed compressional waveform. Fig. 7 shows two superimposed waveforms from the model with a) water level flush with the sediment surface, and b) the sediment covered with a very thick water layer.

Several dispersion measuring methods were evaluated. The author found that the most accurate method to determine the phase velocity dispersion was using a tone burst at a selected frequency, and measuring the wavelength by counting an integer number of wave peaks that passed by a time marker on the oscilloscope as the distance between source and receiver transducers was varied. A procedure was used to achieve the same level of sediment compactness yielding a repeatability of one part in 1000. The distance between the transducers was measured with an accuracy of 0.01 mm over a path length of 30 cm.

The measurements were repeated incrementally at different frequencies between about 70kHz and 880 kHz for each sediment.

The plotted experimental results for the dispersion of high-frequency compressional waves in saturated fine sand, coarse sand, and glass beads are presented in Fig. 8. The dashed lines were calculated from linear regression. The compressional velocity in coarse water-saturated sand *decreased* by 14% as the frequency increased from 80 to 880 kHz, while the Biot theory predicted an *increase* of < 1 %. The velocity in fine sand decreased by 3.6 %, and in the glass beads by 3%. The dispersion results obtained under the current contract confirmed the observation by Guillon et al. [35] of the high-frequency dispersion trend in saturated sand contradicting the Biot theory.

The author examined low-frequency field results obtained by Chotiros [22] from the Kings Bay Experiment measured at two different grazing angles { $\theta = 90^\circ$ and $\theta = 39^\circ$ }. The replotted dispersion results are also shown on the same graph in Fig. 8. The field data velocity decreased by about 6% as the frequency increased from 5 kHz to 60 KHz.

Wingham [26] measured the dispersion of high-frequency compressional waves in water-saturated sand. Wingham's results agreed with the Biot theory as the velocity *increased* by less than 1% as frequency increased from 100kHz to about 380 kHz. Wingham's experimental results [26] did not reveal the high-frequency dispersion trend described in this report. One possible explanation is the fact that Wingham used a bandlimited low-frequency hydrophone. The author digitized the first waveform from Wingham's data [26] and plotted the resulting Fourier Transform shown in Fig. 9. Only 128 points were needed to digitize and represent Wingham's waveform. The resulting spectrum shown in Fig. 9 hints that very little energy was present in Wingham's data between 100-500 kHz.

Several investigations were conducted to double check the dispersion results shown in Fig.8 in view of knowing their conflict with the established Biot theory [30]. Another surprising finding was obtained when the dispersed compressional waveform from a solid block made of sand in paraffin wax had similar dispersion as the water-saturated sand as shown in Fig. 10. No apparent dispersion was observed in either a solid aluminum block or a Plexiglas blocks (bottom two traces in Fig. 10). Koesoemadinata and McMechan [42] provided an empirical formula for the dispersion of P waves in sandstone with the dispersion part following $0.388f$, where f is the frequency in MHz for the frequency range 400 Hz to 1 Mhz. Further research is needed to find the physical mechanism explaining the controversial high-frequency dispersion in water-saturated sediments.

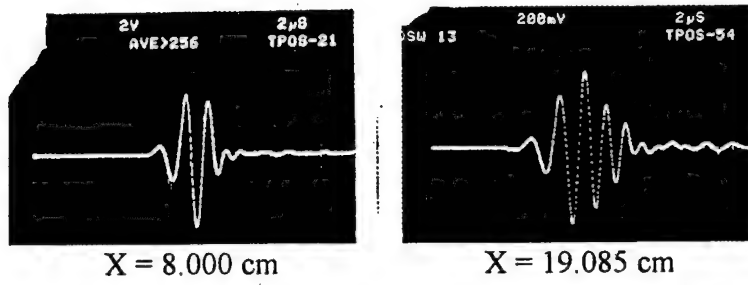


Fig.1. Waveform of dispersed compressional wave in saturated fine sand (Narragansett Beach, RI) recorded at a distance $X = 8.000$ cm and $X = 19.085$ cm.

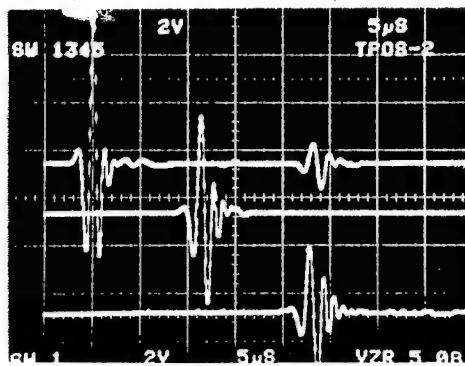
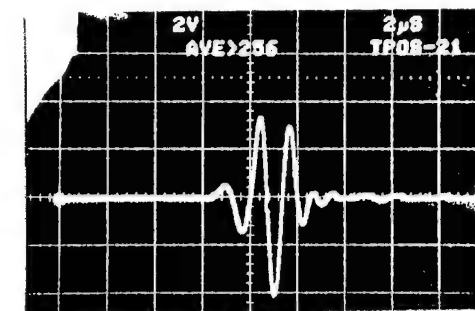
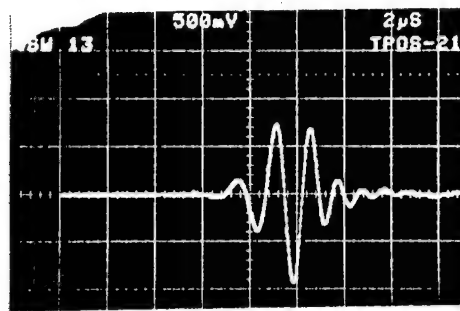


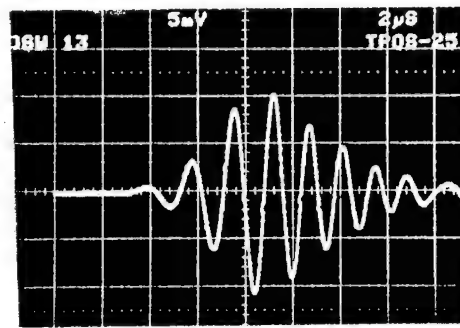
Fig. 2. Compressional wave in saturated glass beads measured at three distances $X = 2$ cm, 4 cm, and 6 cm.



Fine sand



Medium sand



Coarse sand
(750 μm-1.5 mm)

Fig. 3. Comparison of measured dispersed P waves in water-saturated fine sand, medium sand, and coarse sand. Source-receiver distance X = 8.000 cm.

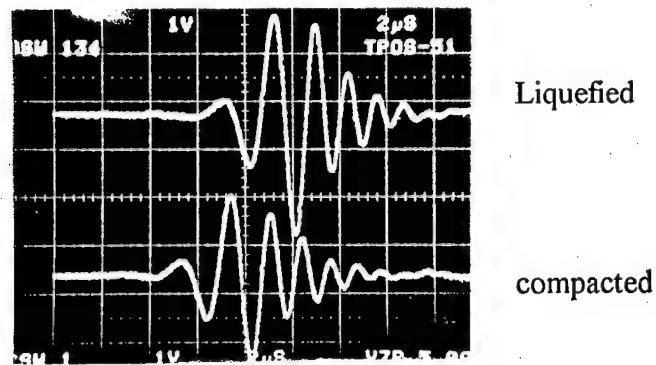


Fig. 4. Dispersed compressional wave in liquefied and compacted underwater glass beads. Compaction was achieved by tapping on the tank wall ($X = 18.639$ cm).

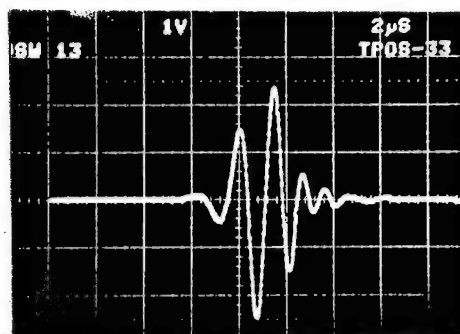


Fig. 5. Vertically propagated dispersed compressional waves in saturated fine sand ($X = 12$ cm).

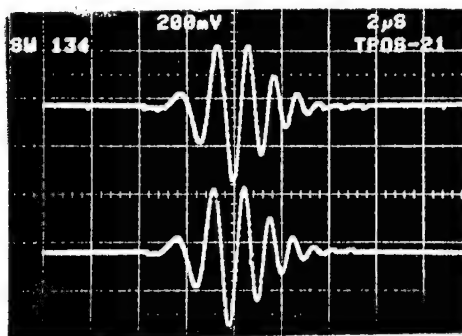


Fig. 6. Effect of depth Z in sediment on dispersion of compressional wave in water-saturated glass beads. Source-receiver distance was fixed $X = 8$ cm.

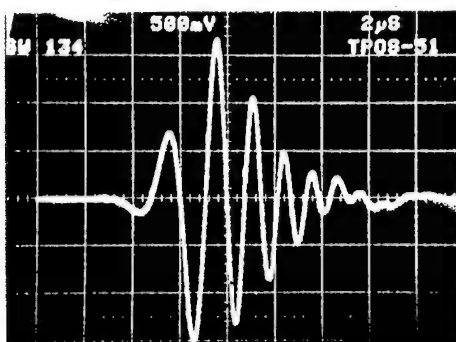


Fig. 7. Identical dispersed waveforms were obtained when the water level "h" was varied. The photograph shows two superimposed traces recorded with $h = 0$ and $h = 15$ cm.

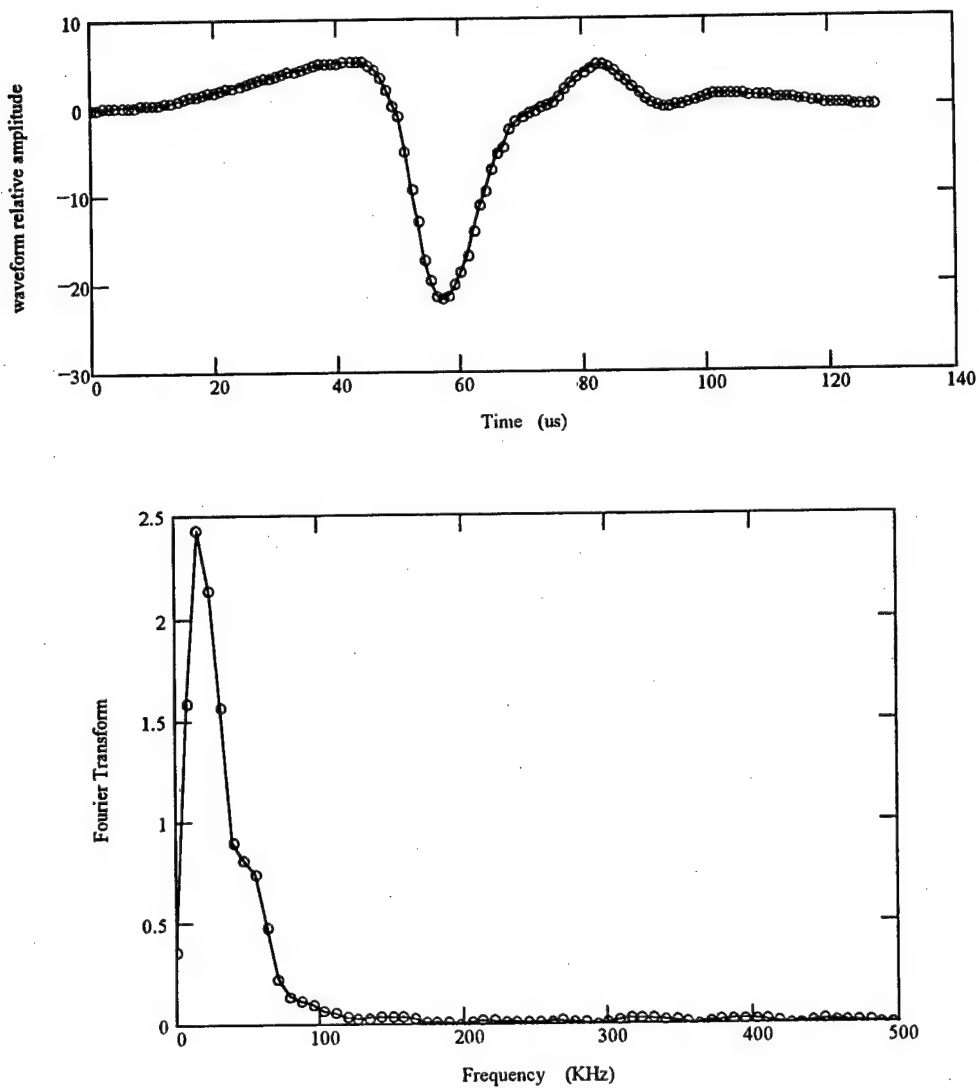


Fig. 9. First waveform from Wingham's data [26] was digitized and replotted together with the corresponding Fourier Transform hinting lack of high frequency energy needed for accurate characterization of the dispersion between 100-500 kHz.

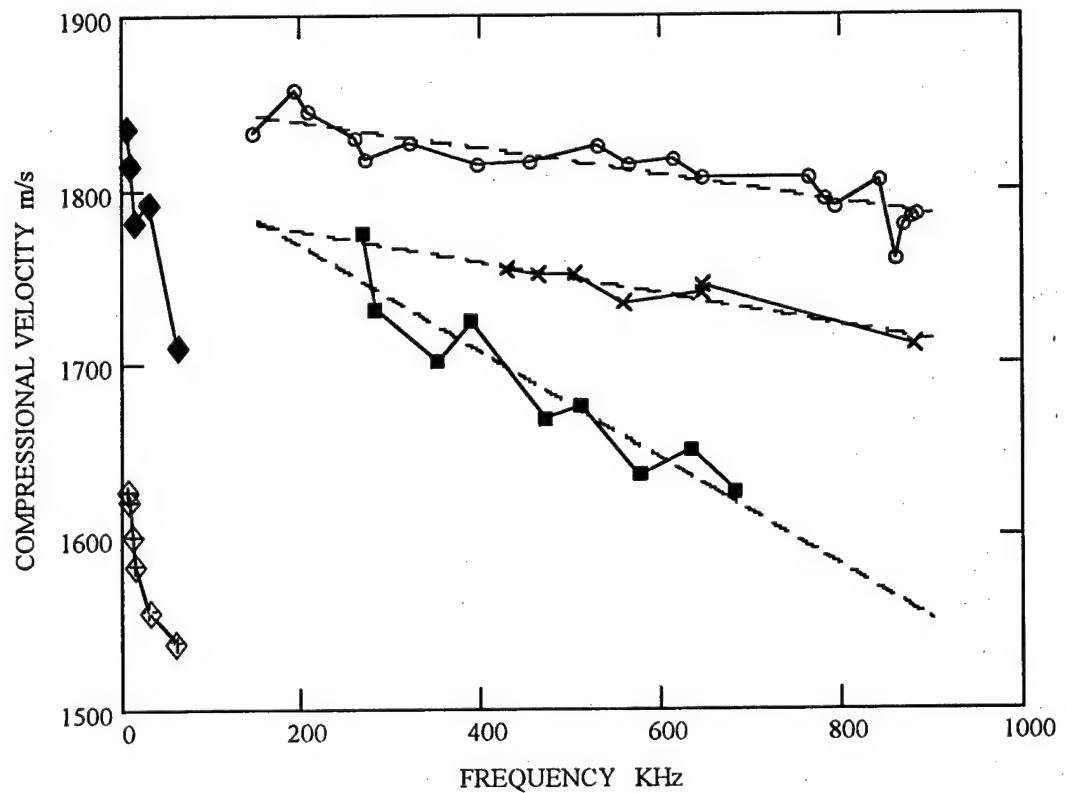
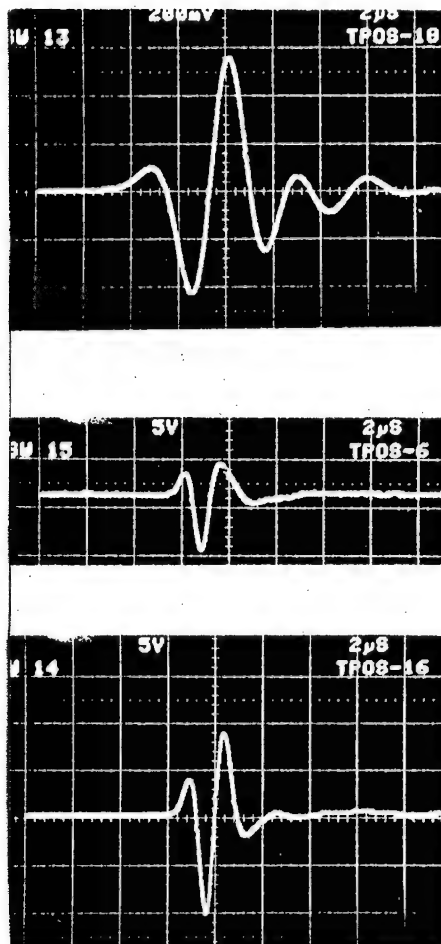


Fig. 8. Measured compressional wave velocity dispersion in water-saturated sediments not explained by the existing theories. The velocity is plotted as function of frequency showing the dispersion in saturated fine sand (---x---), coarse sand (---■---), and black glass beads (---o---). The dashed lines were obtained from linear regression. Low-frequency (5-60 kHz) field data by Chotiros [22] from the Kings Bay Experiment are replotted also indicating a decrease in the compressional velocity as frequency increased recorded at two different grazing angles { $\theta = 90^\circ$ (---◆---), and $\theta = 39^\circ$ (---◇---) }.



Sand in paraffin wax
 $X = 8.7 \text{ cm}$
 200 mV/div.

Aluminum
 $X = 10 \text{ cm}$
 5 V/div.

Plexiglas
 $X = 10 \text{ cm}$
 5 V/div.

Fig. 10. Dispersion of compressional waves propagated in a solid block of sand in paraffin wax (Top) had a similar type of dispersion as the water-saturated sand model. For comparison, nondispersive waveforms were obtained from an aluminum block (Middle) and a Plexiglas block (Bottom) as shown. The source amplitude was reduced by 20 dB in the Aluminum and Plexiglas models.

III. DRAINED SEDIMENT

The previous section dealt with the frequency dependence of the compressional wave velocity C_p in water-saturated sediments. At a given frequency, what is the effect of water content on C_p ? Bachrach and Nur [24] calculated the compressional velocity in sand as function of water saturation based on the low-frequency Biot-Gassmann theory. Their calculated results showed that from 0% to 99% water saturation, C_p remained less than 200 m/s. According to the theoretical model, the last 1% of added water to reach full saturation increases C_p by almost a factor of eight (C_p in water-saturated sand is about 1750 m/s). Jacoby et al. [89] measured the elasticity of frozen partially saturated sand.

Measurements by Velea [43], and Tavossi and Tittman [44] near 10 KHz revealed that C_p in drained sand is about 200 m/s. Shields et al. [45] determined the effect of water vapor on C_p in Ottawa sand and glass beads. The vapor had little effect on the 10 KHz compressional wave in both materials and remained near 200 m/s.

Quantitative experimental results obtained by the author under the previous ONR contract found that the velocity of high-frequency (300 kHz) compressional waves *increased* by about 8 % as the water content was decreased by 18% from full saturation [39-41]. Fig. 11 shows the measured velocity plotted as function of water saturation in fine sand (Kennebunk Beach, Maine), medium sand (play beach sand), coarse sand (Old Orchard Beach, Maine), and glass beads (430-600 μm - Potters Industries P-0203). At 100% saturation, the spherical glass beads (430-600 μm) had a higher compressional wave velocity than the sand (fine, medium, and coarse). The compressional wave velocity increased in all four samples as the water content was decreased. This increase in velocity is not explained by existing theories and is in contrast with the Biot-Gassmann theory which predicts that the velocity of low-frequency compressional waves *decreases* by 85% as the water content is decreased by only 1% from saturation.

Broadband dispersed waveforms of P waves from two other saturated and drained models are displayed in Fig. 12. One model consisted of black glass beads (0.25 mm), and the other was coarse sand (750 μm -1.5 mm). The source was excited with a single broadband pulse. The waveforms were recorded with the source-receiver separated by $X = 8$ cm. The top and bottom traces in Fig. 12 correspond to the saturated and drained models, respectively. The drained models were dried with a sponge and tissue paper to interrupt the water/water molecules connectivity. Fig. 13 shows a photograph of sharp corners of a carved cylindrical cavity on the surface of drained black glass beads demonstrating the stiffness of the drained sample (water-saturated glass beads has no rigidity and cannot be carved). Time-dependent stiffening was observed after draining fine sand. The shear wave velocity increased from 97 m/s at the time $t = 10$ minutes after draining to 118 m/s at $t = 60$ minutes (Fig. 14).

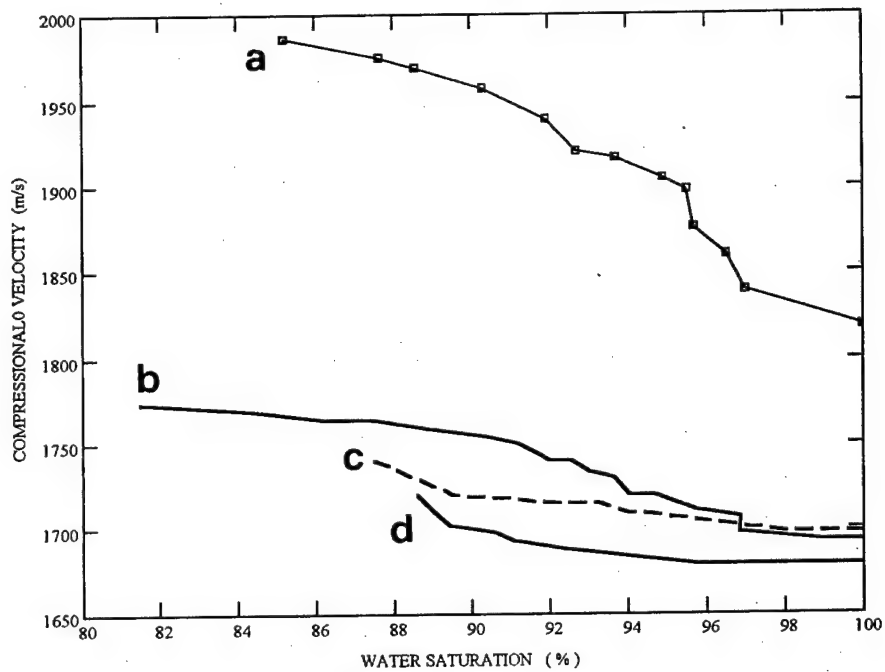


Fig. 11. Measured compressional wave velocity as function of water saturation [41] in various models. From top to bottom: a) Glass beads (430-600 μ m- Potters Industries P-0230), b) Coarse sand (Old Orchard Beach, Maine), c) Medium sand (Play beach sand), d) Fine sand (Kennebunk Beach, Maine).

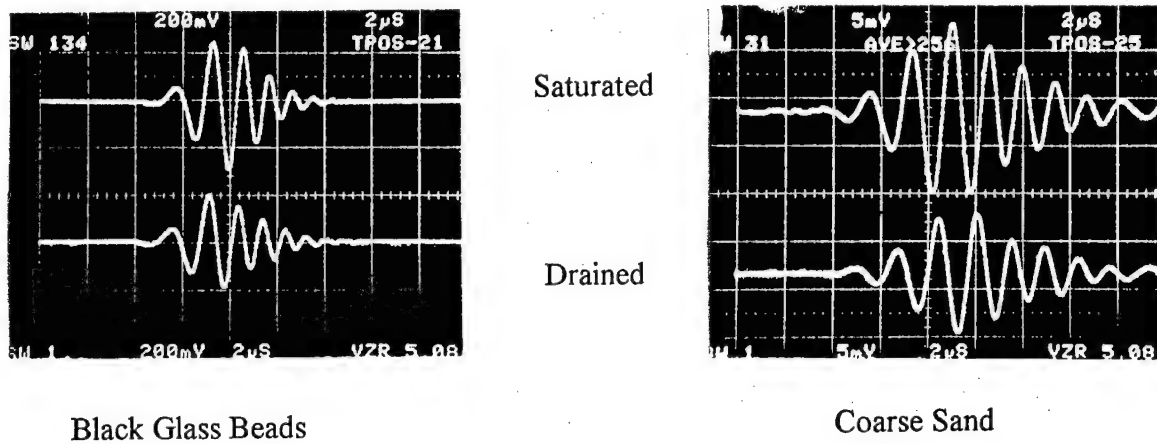


Fig. 12. Comparing dispersed waveforms of P waves in saturated and drained beads and coarse sand models. After draining the water, the glass beads and the sand were dried with a sponge and tissue paper. (X = 8 cm).

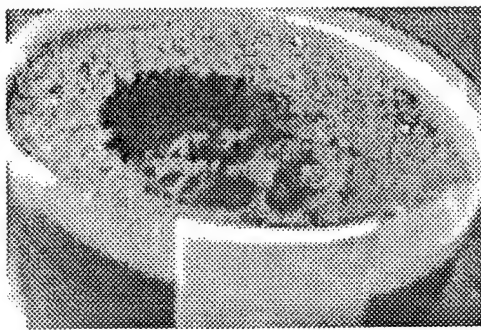


Fig. 13. Photograph of drained black glass beads in plastic container. A cylindrical cavity was carved on the surface of the drained beads to demonstrate its rigidity. Water-saturated glass beads has no rigidity and cannot be carved.

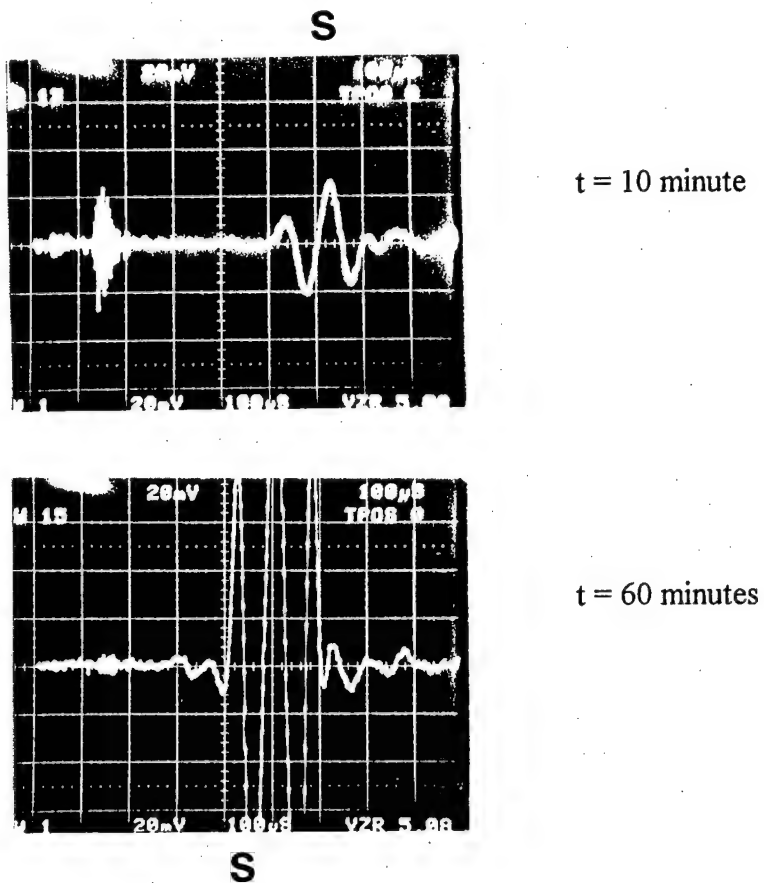


Fig. 14. Time-dependent stiffening was observed in drained fine sand. The shear wave velocity increased from 97 m/s at $t = 10$ minutes after draining to 118 m/s at $t = 60$ minutes. Shear piezoelectric transducers were used to generate and detect the ultrasonic waves. ($X = 4.1$ cm).

IV. CAPILLARY CAVITATION AND CRYSTALLIZATION

Currently, there are no theories available capable of predicting the high-frequency wave velocities and attenuation in unsaturated marine sediments. In order to predict the seismoacoustic response of the seafloor under various conditions, it is essential to understand the sediment grain to grain coupling mechanisms at the microscopic level. Little is known about the properties and effect of the thin seawater film trapped between the grains. Theories on elastic wave propagation assume that shear waves cannot be transmitted across a water layer sandwiched between two solid surfaces. The Buckingham theory [12, 20, 32] depends on grain roughness, where the shear wave speed goes to zero as the losses vanish. In Buckingham's model, grain shearing introduces rigidity which in turns supports a shear wave.

It is well known that two parallel wet glass plates stick together when pressed against each other. A preliminary investigation of the "suction-cup effect" was undertaken to study some aspects of seawater grain to grain adhesion and shear coupling in the "absence of roughness". On the theory of tackiness, Gay and Leibler [46] described the role of the suction-cup effect in adhesive polymer films as increasing the bonding strength by up to 10,000 times. Later work by Creton et al. [47] indicated that the suction cup effect contributed only a very small part to the energy of debonding due to the very peculiar properties of deformability of the adhesives.

The seemingly simple "suction-cup effect" problem unveiled a series of complex mechanisms on solid-like behavior of confined liquids, confined crystallization, cavitation of trapped water film, tapered capillaries, nanofiltration and desalination, formation of rings and seals, water trapping, time-dependent stiffening, and loading hysteresis as explained below. In this section, a series of photomicrographs are presented providing physical insight into hidden capillary mechanisms on cavitation of a seawater film between two glass microplates. Ultrasonic shear wave coupling between two smooth glass plates bonded by capillary forces and crystallized salt is demonstrated.

Visualization Studies and Background on Related Issues

The effect of capillary phenomena is significant for flat surface configurations. Aracne-Ruddle et al. [48] found that the acoustic properties of sediments are sensitive to clay content at low pressures. Their ultrasonic results indicated some unexplained surprising time-dependent behavior of the shear wave. Clay consists of smooth hexagonally shaped crystalline platelets about $1 \times 1 \times 0.1 \mu\text{m}$. Beach sand grains are angular and have flat surfaces contributing to capillary adhesion in unsaturated sediments.

The London-van der Waals force of interaction between two parallel plates in vacuum follows the inverse third-power law according to the London-Hamaker theory, where the force is proportional to $1/d^3$ and d is the distance between the plates. Howe et al. [49] described the London-van der Waals force for the interaction of a sphere and a plate as proportional to $1/d^2$. The interaction force of a 1mm diameter glass bead and a plate is in

the order of 10^{-5} N for $d \sim 25$ angstroms, and increases rapidly as d decreases. At a separation of 5 angstroms, the force is about 80×10^{-5} N.

The Laplace-Young equation [50] of capillarity

$$\Delta P = \gamma (1/R - 1/r) \quad (1)$$

relates the pressure difference across a curved interface to the surface tension and the radii of curvature. ΔP is the pressure difference across the gas water interface, γ is the surface tension, R = radius of curvature, and r = second radius of curvature. A spherical interface is a special case when the pressure difference is equal to twice the surface tension divided by the radius. As the radius of curvature of the interface becomes infinite like a flat surface, the difference in pressure on the two sides decreases to zero. Small cavities (bubbles) have a small radius of curvature creating a large pressure difference across the interface. The equation is used to predict the meniscus forces and assumes the surface tension γ to be constant. The surface tension of water is $\gamma = 72.8 \times 10^{-3}$ N/m.

Equations for estimating meniscus forces and viscous forces were obtained from references [51-52]. McFarlane [51] gave the equation for the meniscus force between two flat surface with a surface area "A" and a fluid layer of thickness h . The Laplace pressure draws the plates together with the force.

$$F = (2A\gamma\cos\theta)/h \quad (2)$$

where θ is the contact angle. The capillary force equation between two spherical grains was described by Likos and Lu [53].

Is the Laplace-Young equation valid for a confined nano-film between two *touching* plates? The answer to this question is not known.. Sobolev et al. [54] found that the surface tension in cylindrical capillaries with a diameter as small as 80 nm was the same as the water bulk surface tension value. Megaridis et al. [55] studied the behavior of pressurized fluids in carbon nanotubes with a diameter of only about 50 nm.

Van der Veen et al. [56] showed that when an ultrathin liquid film is confined in nanometer gaps between two solid surfaces, the liquid molecules become ordered giving rise to solid-like properties and causes the surfaces to stick. This is different from the well known time-dependent interfacial viscous force described by Stefan's equation [57-58] based on a viscosity that does not dependent of the layer thickness.

$$F = \frac{3\eta\pi R^4}{4t} \left(\frac{1}{H^2} - \frac{1}{h^2} \right) \quad (3)$$

where, η = viscosity, R = radius of fluid disc between plates, t = time, H = initial fluid thickness, h = final fluid thickness.

One point of interest is understanding the instability of a confined ultrathin water layer in the presence of heterogeneous nucleation and cavitation in tension and shear. Archer et al. [59] observed that a liquid can fracture like a solid forming a vacuum cavity above some critical shearing rate. Microbubbles in seawater dissolve because the pressure inside the bubble is greater than the pressure in the water. The behavior of a shearing cavitation bubble confined between two plates is not known. Microbubbles trapped in an ultrathin capillary channel cannot be removed by suction because the pressure exerted by the capillary forces can far exceed one atmosphere. Any air bubbles entrained in a cylindrical capillary channel create a vapor lock. Degassing underwater sediments can remove only the large bubbles but not the bubbles trapped in channels narrower than $0.9 \mu\text{m}$. Evans [60] reported on the properties of liquids confined between two hard walls stating that when the walls are close enough to each other cavitation occurs and the liquid evaporates. Furthermore, Evans stated that confinement shifts the condensation or freezing point. When the dimensions of the capillary channel is microscopic, the local density of the fluid differs from that of the bulk due to the confining effect of the walls citing clays as an example. Maeda [63] discussed capillary freezing and the change of the mechanical properties from liquid-like to solid-like as the distance between two walls were changed.

Visualization studies were conducted to observe the behavior of a thin seawater film between two glass plates under various conditions. The experiments were conducted using 0.13 mm thick glass microplates by Corning No. 0211. These 3.5x5 cm microplates were very smooth (27 to 58 Angstroms peak to valley over an area of $0.357 \times 0.269 \text{ mm}^2$). The properties of the Corning 0211 glass are: density $\rho = 2.53 \times 10^3 \text{ kg/m}^3$, Young's modulus $E = 7.44 \times 10^{10} \text{ N/m}^2$, shear modulus $G = 3.003 \times 10^{10} \text{ N/m}^2$, and Poisson's ratio $\sigma = 0.22$.

An advancing capillary water film can entrain air pockets. Time-lapse photographs showed the formation of entrained circular and elongated air pockets (Fig.15). Trapped air microbubbles always exist between dry sand grains when water is added. This fact may explain why the compressional velocity C_p measured by the author in drained glass beads ($\sim 1750 \text{ m/s}$) was much greater than the 550 m/s measured by Shields and Sabatier [45] when they introduced water vapor to cover dry sand with 16 monolayers. Starting with saturated sand and ending with 16 monolayers by removing water would have resulted in a greater C_p value. Fig. 16 shows a capillary water film advancing between two glass plates that were previously bonded with the residue of an evaporated tap water film forming an island. Newton interference rings were observed in the left photograph before introducing the water. The advancing water film initially could not penetrate the thin gap surrounding the island (first interference fringe) and formed a curved water front, as seen in the middle photograph (Fig.16). It is interesting to note that even after total wetting (right photograph), faint interference Newton rings and microbubbles could still be observed.

Equation (2) indicates that the capillary force increases as the gap between the two plates decreases. Below a critical water film thickness, the capillary forces can exceed the tensile strength of the water and cavitation occurs as the water film ruptures.

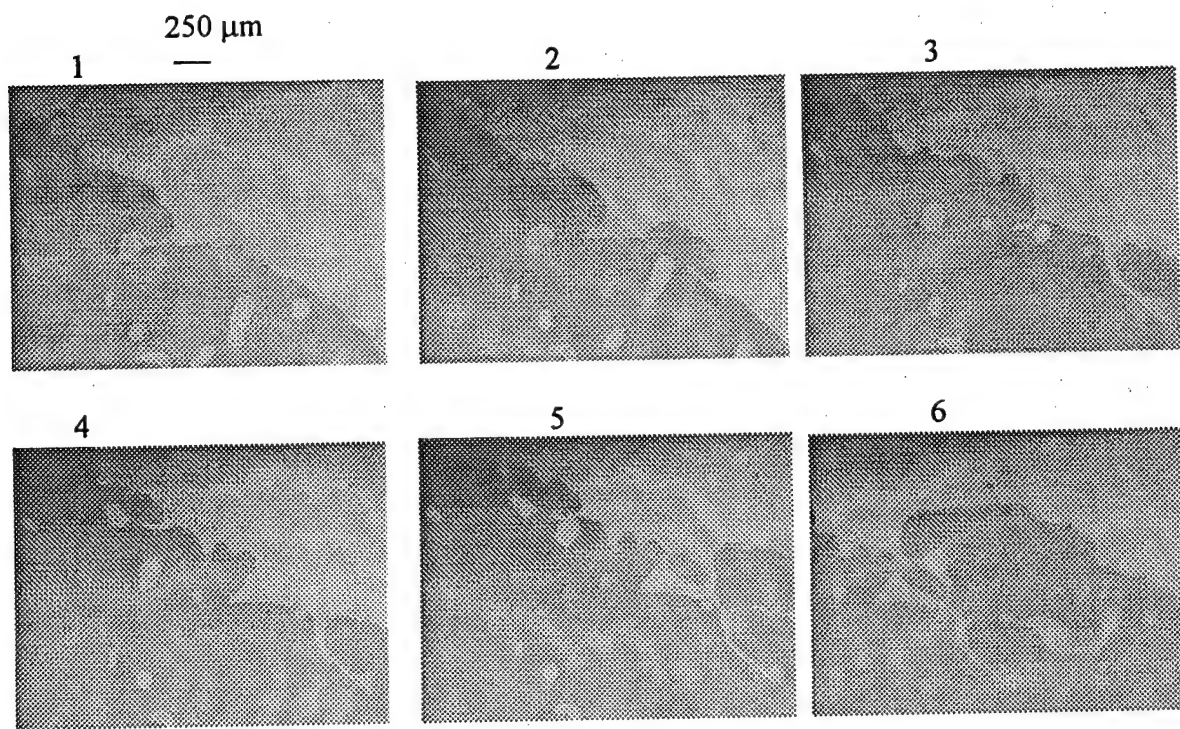


Fig. 15. Time-lapse photographs showing formation of trapped circular and elongated air pockets by an advancing wetting capillary water film between two glass plates. (Magnification 60X).

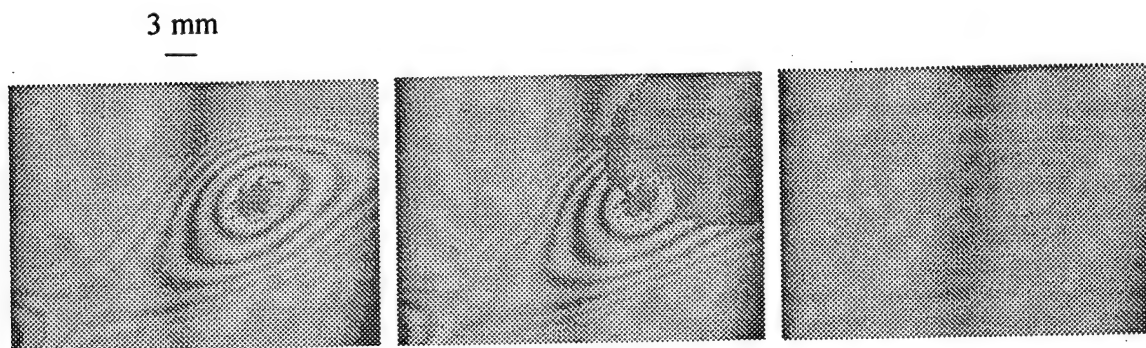


Fig. 16. Progression of the wetting process of an advancing capillary water film interacting with an aged trapped semi-crystallized seawater film. Initially, the advancing capillary water experienced resistance to penetrating the thin channel surrounding the trapped island as indicated by the curved water front in the middle picture. Even after total wetting, interference Newton rings were still observed momentarily (right picture). Complex mechanisms took place related to time-dependent acoustic properties of marine sediments. (Magnification 10X).

Briggs [62] noted the limiting negative pressure of water. The record tension was 270 atmospheres at 10°C. Water impurities determine the ease of cavitation and formation of microbubbles. Chahal an Yong [64] studied the tensile strength properties of water in porous rocks. Seawater contains heterogeneities acting as nuclei and the water can rupture well below its tensile strength. In some models, localized interference patterns were observed through the glass microplates before the occurrence of cavitation (Fig. 17).

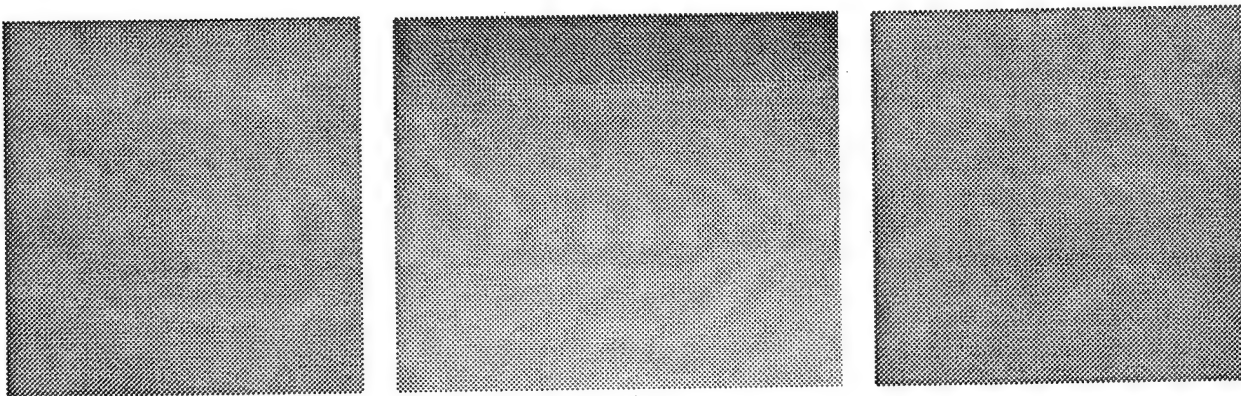


Fig. 17. Localized interference patterns observed in some models before cavitation occurred. (Magnification 60X).

Various cavitation shapes and sizes were observed in trapped seawater film between microplates (Fig.18). Their size ranged from 200 μm to 3 mm in diameter. Noncircular elongated and triangular cavities are displayed in Fig.19 and Fig.20. In the ocean, cavitation bubbles collapse violently and oscillate creating high pressure and high temperature. In contrast, capillary cavitations between two plates do not exhibit oscillation. Or and Tuller [63] analyzed cavitation during desaturation of porous media under tension caused by heterogeneous nucleation.

Chikina and Gay [65] estimated the size of the region influenced by one bubble assuming horizontal film deformation as more bubbles appear. The bubbles remain at a distance greater than $d = h/(1-2\sigma)^{1/2}$, where h is the film thickness and σ is Poisson's ratio. Chikina and Gay stated that the nucleation of new bubbles reduces the stress in the film preventing the formation of new bubbles. Initial rupture creates a vacuum cavity which becomes later a vapor bubble. Water has a vapor pressure of 2.34 kPa at room temperature and 101.6 kPa at 100°C. Between the glass plates, several small cavitation bubbles develop. As the bubbles grow, they may merge creating larger bubbles. The bridges connecting the bubbles break up leaving multiple isolated water droplets. Using high speed video microphotography, Williams and Barrow [66] observed the growth of a cavitation bubble from negative pressure in a 0.1-1 μm thick liquid film confined between a sphere and a plane surface. The rupture of a confined thin liquid film by thermocapillarity was reported by Smith and Vrane [67]. Chen and Israelachvili [68] and Kuhl et al. [69] observed the formation of cavities in a thin liquid film between two mica surfaces when the surfaces were pulled apart beyond a critical velocity.

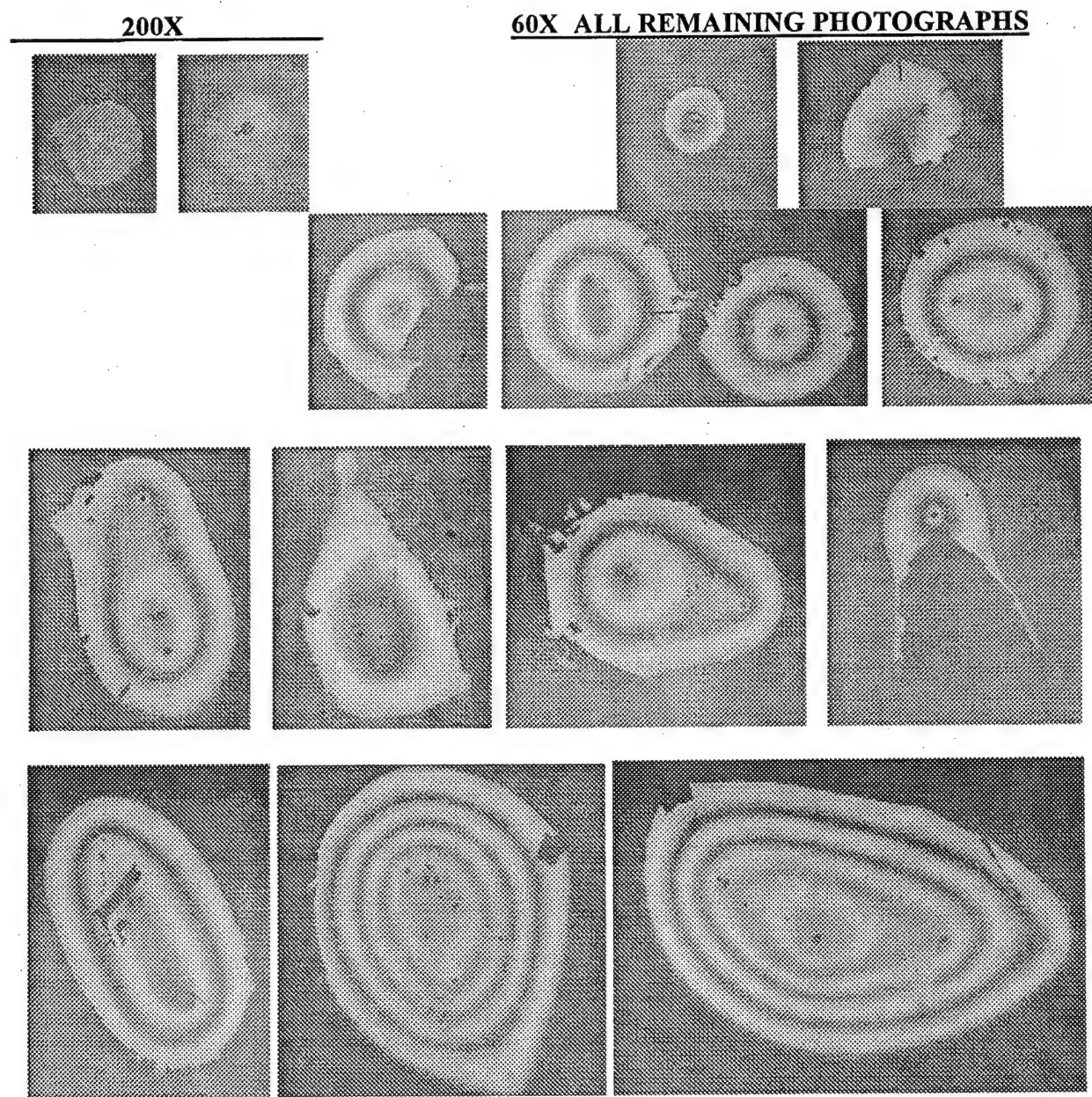


Fig. 18. Various shapes and sizes of cavitations in trapped seawater film between two Corning microplates. The trapped seawater layer was behaving sometimes like a liquid and sometimes like a crystallized solid. The cavitation diameters shown are between 200 μm and 3 mm. (Magnification 60X except for the first two photographs 200X).

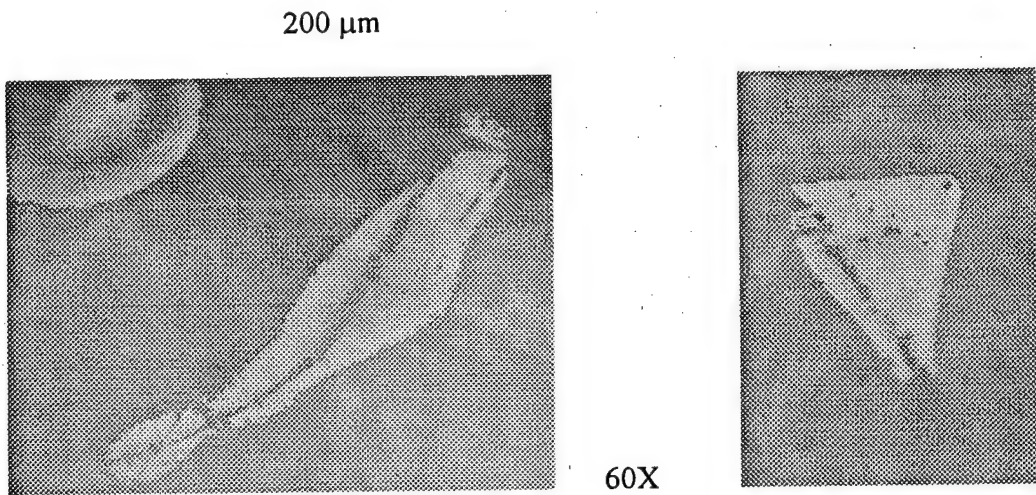


Fig. 19. Noncircular cavitations were observed in several models when the water separated from crystallized regions not exposed to the atmosphere.

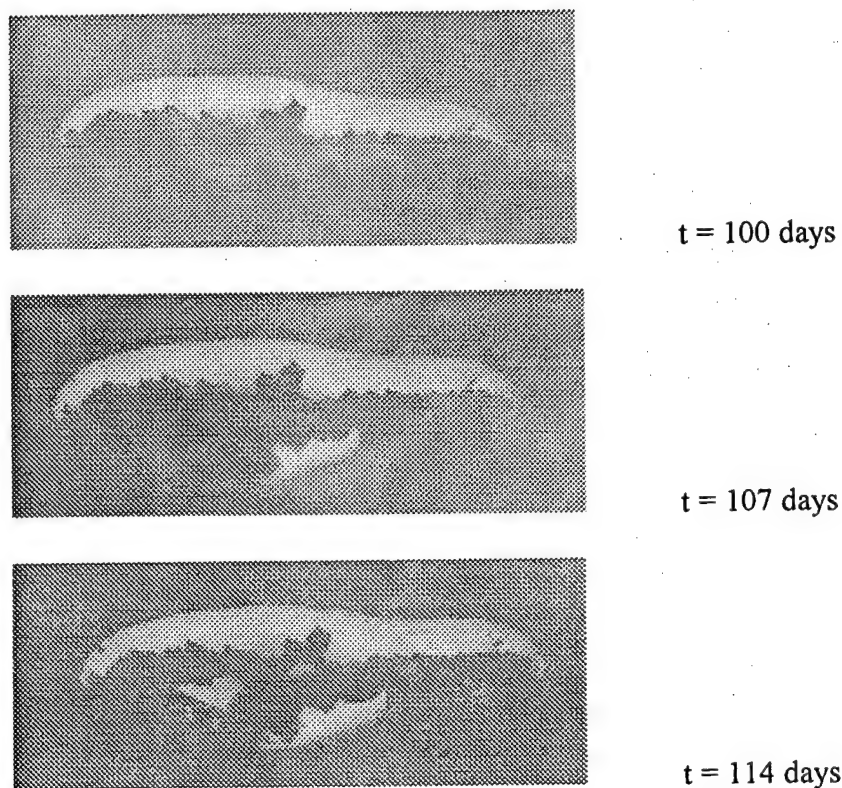


Fig. 20. An elongated cavitation rupture (2 mm long) formed between the trapped seawater film and an inner crystallized region observed 100 days after the model was allowed to dry. The other two pictures were taken one week and two weeks later after the formation of the initial elongated feature showing the slow evolution and change in the trapped mesoliquid. (Magnification 60X).

The capillary seawater thin water film was trapped for several months between the glass microplates partially due to the formation of a seal from the salt and other impurities in the seawater. Renard and Ortoleva [74] introduced a model explaining the existence of a trapped fluid film at grain contacts. It was initially surprising to find the seawater film trapped for almost a year. A literature search provided an *extreme* example on Zolensky's discovery of a brine solution in a halite salt crystal trapped in the 1998 Monahans meteorite for about 4.5 billion years predating the sun [73].

The trapped water film had its outer edge connected to the ambient atmosphere, while the inner border was facing the cavitation vapor bubble. Different types of edges and crystallizations were observed (Fig.21-Fig.26) at the water/air boundary: a) formation of sharp 90° cornered water pools (Fig. 23), b) sharp rectilinear crystallized edges with 90° angular steps (Fig. 21-22), b) cracked film edges (Fig. 21), d) multiple crystallized parallel contours connected by bridges (Fig.24), e) fine granular salt particles were observed without the formation of large crystals in the inner regions of a cavitation, and f) X-shaped crystals formed inside the wet region when heated (Fig. 26), and g) dendritic crystallization (Fig. 25). Anderson [86] found that when sodium chloride crystallizes in the presence of biological matter a dendritic form of crystallization develops instead of the cube shaped crystals. Seawater is a solution of NaCl, MgSO₄, Mg Cl₂, and CaHCO₃. Seawater is at 10% of the saturation point. The solubility of salt at 20° C is 37 grams per 100 ml of water.

The seawater film between the microplates evaporated more slowly as time progressed resulting in time-dependent acoustic properties (Fig. 22). The effect of time-dependent mechanisms in sediments and aging is not well understood. Denisov and Reltov [70] measured the change in the adhesion of sand grains on a glass plate for different soaking and drying time. Their experiments showed the shear bonding increased by more than 300% for grains submerged for 14 days and dried for 20 hours. Mitchell and Solymer investigated time-dependent strength gain in freshly deposited or densified sand [71]. Losert et al. [72] reported on gradual slow strengthening of wet sand under low pressure. There are several mechanisms responsible for increasing the shear modulus of sand.

Abrupt formation of circular cavitation pockets in aged trapped seawater film between the microplates occurred simply by locally stressing one of the plates surface. Fig. 27 shows the water film before and after the generation of such a stress induced cavitation. The trapped seawater film between the Corning microplates did not seem to evaporate when the bonded plates were placed in the oven at 200° C. Faint X-shaped salt crystals appeared when the oven temperature was raised to 350°C (Fig. 26). No seals were formed when distilled water was used instead of seawater.

In an experiment on ring formation, a circular drop of salt saturated water (4.75 cm diameter) was placed on the surface of a glass plate to evaporate. A salt ring formed after the water dried. The weight of the salt in the formed ring was 0.409 g, while the salt covering the entire circular area was only 0.166 g. The water thickness decreased as the water evaporated, and the salt kept on migrating to the pinned perimeter. Deegan et al

[75] studied ring formation from the preferential deposition of a solute at the contact line of drying solution on a flat surface exposed to the atmosphere. Multiple ring formation in a drying Latex film due to pinning-depinning events was reported by Shmuylovich et al. [76].

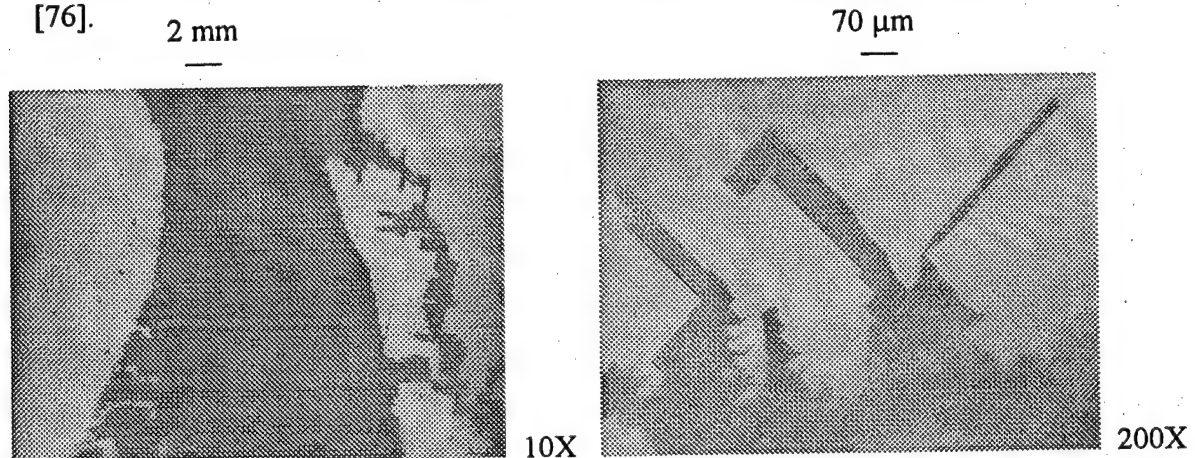


Fig. 21. The left photograph (10X) compares the edge of the trapped seawater film facing the cavitation side (Left) to the crystallized edge facing the atmosphere (Right). The photograph on the right shows a magnified view (200X) of the crystallized right edge. The water film snapped and separated from the pinned elongated crystallized right edge explained by equilibrium of forces between water adhesion to the crystallized salt and the capillary force acting on the shrinking evaporation water film. Cracking behavior was observed in the seawater film facing the cavitation side.

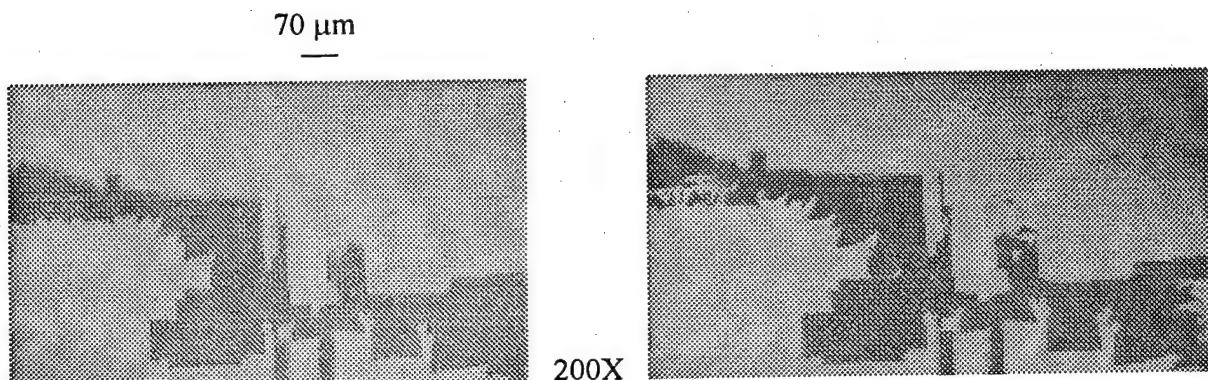


Fig. 22. Trapped seawater regions between the glass plates that appeared completely crystallized were not. The two photographs were taken 5 days apart showing slow changes associated with water evaporation and confined crystallization.

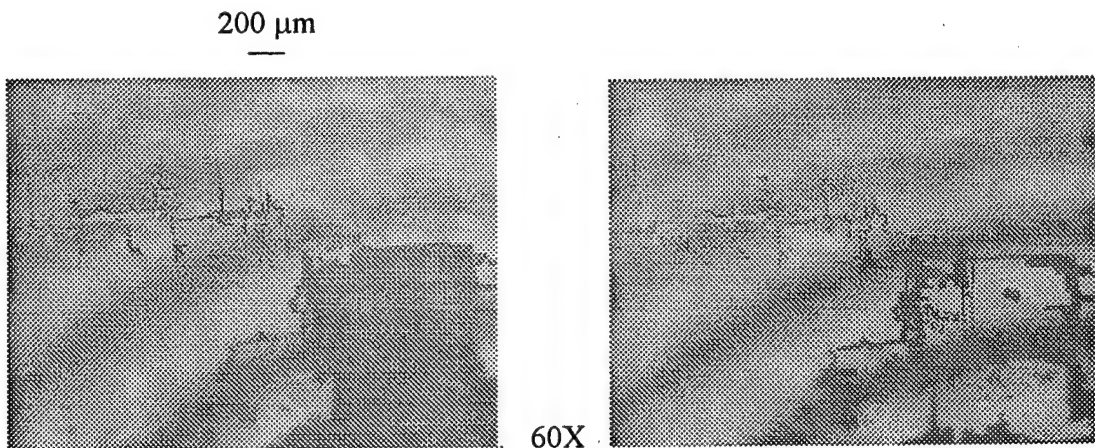


Fig. 23. Slow formation and evaporation of sharp edged (90°) rectangular seawater films were observed leaving complex salt crystallized borders. The photographs were taken one week apart of the same region. Time-dependent shear wave coupling between the two smooth microglass plates holding the seawater film depended on confined crystallization mechanisms. (Magnification 60X).

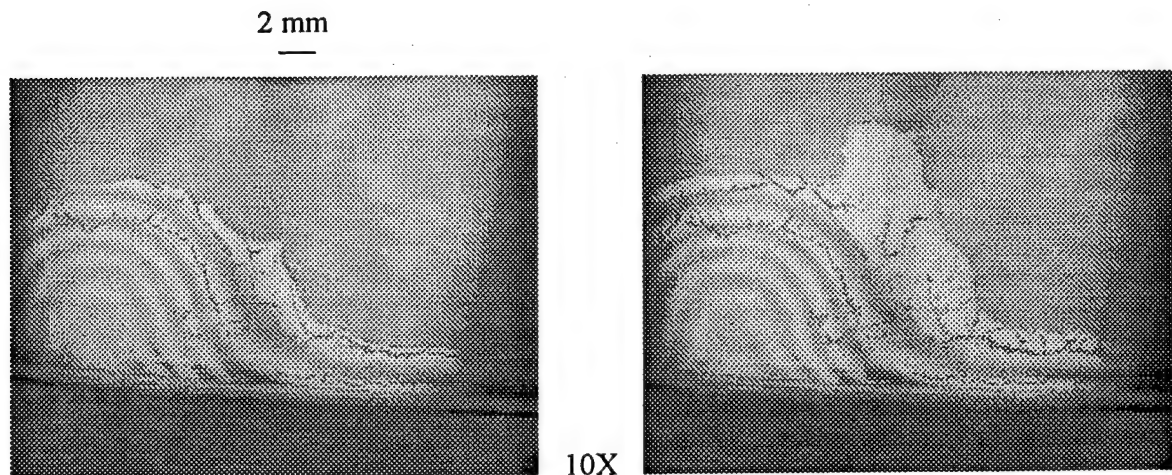


Fig. 24. Multiple parallel branched crystallized edges were formed tracing the capillary seawater film (gray region) contour during evaporation of the water. The film was subjected to increased tension with evaporation until the water film snapped and separated from the crystallized salt along its border. The water retreated rapidly over a short distance without forming a crystallized border. The process was repeated when a new pinned crystallized border had a chance to develop. The pictures were taken 72 hours apart.

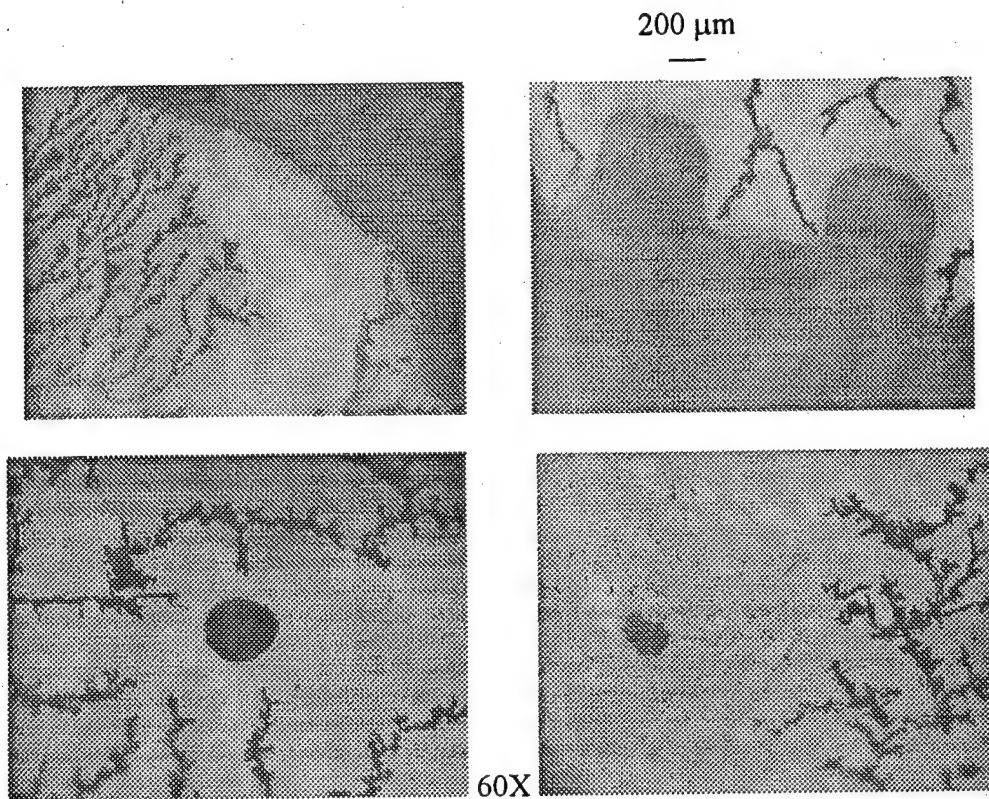


Fig. 25. Crystallized dendritic forms were observed in some models. The crystallized edges did not always continue to make contact with the receding water boundary and ended abruptly due to either rapid water retraction or microfiltering between the plates. Complicated equilibrium forces took place controlling the water edge shape and crystal growth. The remaining water film either evaporated leaving a fine powder or it formed an inner trapped pool.

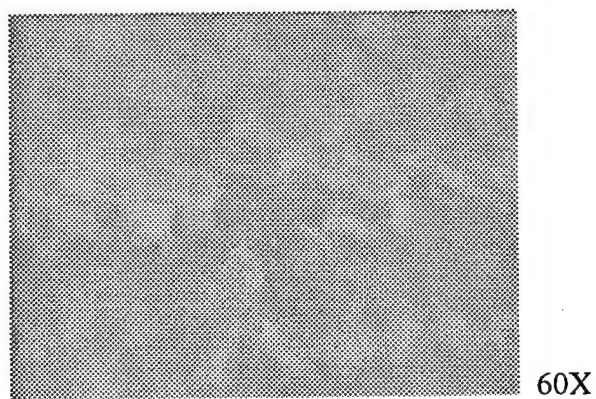


Fig. 26. Faint cross shaped thin salt crystals were formed when the 6 months aged seawater film between the glass plates was placed in the oven at 200°C for 15 minutes.

As water evaporated, salt crystals were formed along the outer edge of the water film fixing the gap between the plates at that point. Further evaporation caused the plates to bend and the gap decreased away from the crystallized border forming a tapered capillary configuration. In 1924, Bouasse [77] observed that when a water drop was placed at the bottom large-end of a tapered conical tube, the water drop moved up to the open tip driven by the difference in capillary Laplace pressure. A water film always moves towards the thinnest gaps. The tapering increased the capillary force pulling the water film away from the outer crystallized edge. The water separated from the thick crystallized edge with a snapping action.

It is interesting to note that as the seawater passed by tapered narrow channels, filtration and desalination took place at different stages (microfiltration 0.1 μm gap, ultrafiltration 10 nm gap, and nanofiltration 1 nm gap). Although the Corning microplates are highly polished, it is difficult to estimate the exact area of real contact. Persson et al. [78] compared results of an exact analytical model and numerical results on elastic contact between randomly rough dry surfaces. Persson's theory showed that including the lateral interaction between the surface roughness, asperities reduces the area of real contact by a factor of $2/\pi$ compared to the theory of Bush et al. [79]. Halsey and Levine [80] indicated that the force between two rough spheres depends on the amount of water present and the strength of the capillary bridges controlled by surface roughness.

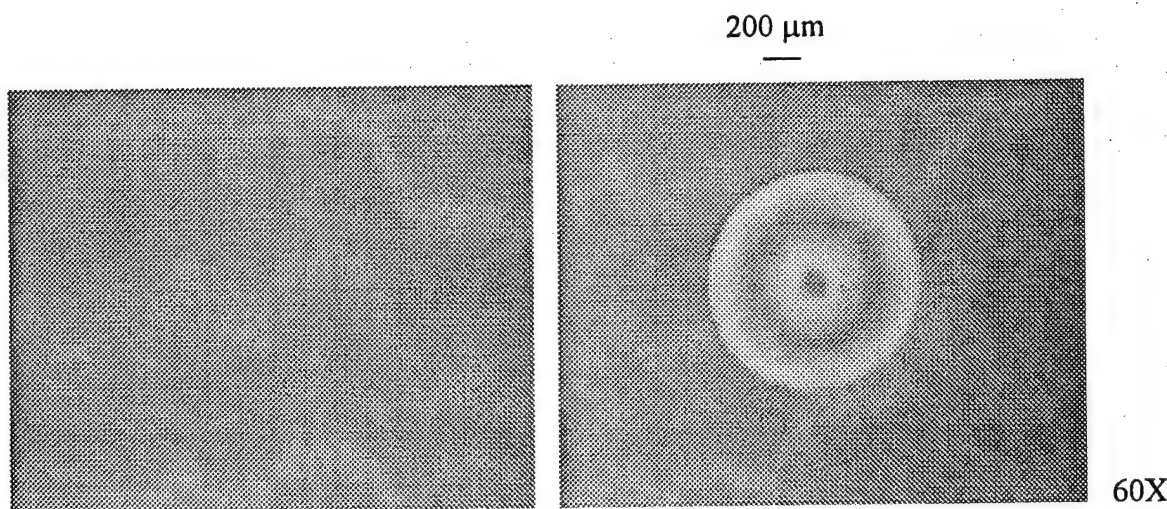


Fig. 27. Instant formation of new cavitation in seawater film trapped for over six months between two Corning microplates. The first picture shows a region of the water film before cavitation. The second picture shows the instant formation of a new cavity by simply pressing locally on the surface of one of the two plate. The instant formation of a circular cavity seems to indicate the presence of a trapped liquid that did not dry yet.

Ultrasonic Shear wave Coupling

The previous section visualized the complex hidden world at the microscopic level of phenomena controlling the time-dependent elastic wave coupling between two solid surfaces trapping a cavitated capillary seawater film. This section presents preliminary experimental results demonstrating ultrasonic shear wave coupling between regular glass microscope slides (1x25x76 mm) bonded with a cavitated capillary seawater film.

Several experimental models were prepared by bonding two glass plates (microscope slides) with a capillary seawater film. Initially, the water film covered the entire surface of the plates. Overnight drying resulted in the formation of cavitations and crystallized features. Salt crystals have acoustic properties close to sand grains and can create strong shear wave coupling. Ultrasonic waves in monocrystals of NaCl in the form of rectangular bars were reported by Belomestnych and Karpova [81]. The lattice parameter for NaCl was given 5.63874×10^{-10} m, and density 2.16×10^3 kg/m³. The compressional wave velocity in the (100) direction 4.77×10^3 m/s and 4.17×10^3 m/s in the (110) direction. The shear wave velocity (100) was 2.43×10^3 m/s.

After a period of six months, some of the models appeared to contain a localized trapped water film surrounded by crystallized edges. The plates were well bonded to each other. The tensile force measured to separate the two bonded plates was about 11% greater than the force based on the suction cup effect alone. Fig. 28 shows the interference pattern in one of the bonded models. It took a shearing load of 13.2 kg to separate the plates.

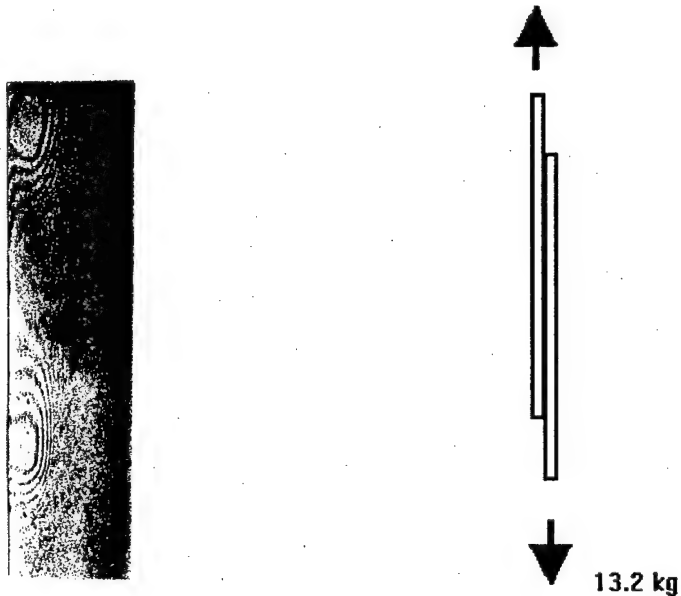


Fig. 28. Interference fringe pattern observed in two glass plates bonded together with a cavitated seawater water film trapped for 6 months. A shear load of 13.2 kg was attained before the bonding strength was surpassed.

Two identical source and receiver piezoelectric shear wave transducers were epoxied to the surface of a 2.2 cm thick Plexiglas block to delay the transmission and detection of shear waves through the models. Fig.29 shows the experimental setup configuration. A single broadband pulse was used to excite the source transducer. The shear wave detected from one of the models is displayed in Fig. 30 (a). This model was aged for a period of six months. A strong shear wave was coupled across the cavitated capillary film with no load applied. When the plates were immersed in water, the shear wave remained (Fig. 30 (b)). A blade was used to separate the immersed plates and create a sliding contact. This caused the shear wave to vanish (Fig. 30(c)). By placing a 15 kg load on the mating wet plates, the shear wave appeared having about the same magnitude as the waveform in Fig. 30 (a).

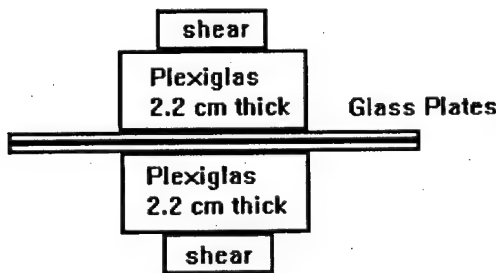


Fig. 29. Generation and detection of shear waves in two parallel glass plate models.

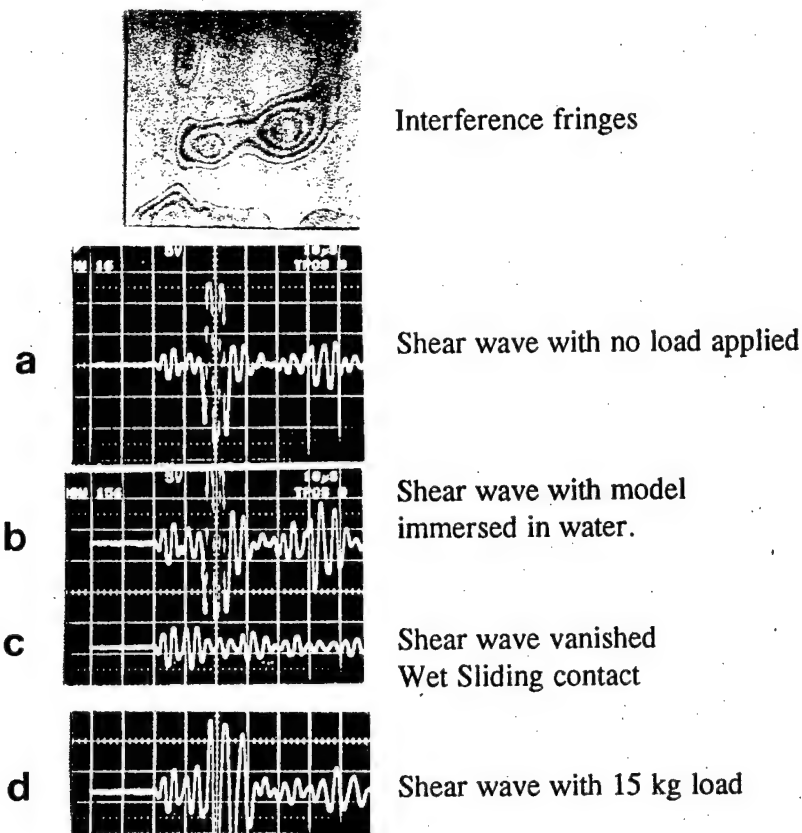


Fig. 30. Detected waveforms from two glass plate model with cavitated capillary seawater film trapped for six months.

Experimental results from another model aged only 24 hours are shown in Fig. 31. A strong shear wave was detected from the bonded plates (Fig. 31(a)). Unlike the previous example, the shear wave disappeared when the plates were immersed in water (Fig. 31(b)). It required a 35 kg load placed on top of the sliding plates to restore the shear wave amplitude as shown in Fig. 31 (c) for the dry contact case, and Fig. 31 (d) for the wet plates condition. The shear wave disappeared when the 35 kg load was removed (Fig. 31(e)).

Loading hysteresis was observed in coupling shear waves. A minimum loading force F_{min} had to be surpassed to reach irreversible adhesion between the wet glass plates. When a 100 kg load was used, the shear wave remained after the removal of the load. It was observed that cyclic loading increased the adhesion-time after unloading. Fig. 32 (a) shows the strong shear wave left after removing a 100 kg load that was cycled four times squeezing a new seawater film held between the plates. The shear wave amplitude decayed slowly with time after unloading. The waveform recorded one hour after removing the load is shown in (Fig. 32 (b)). In this experiment, the shear wave was coupled by capillary forces without the presence of crystallized salt.

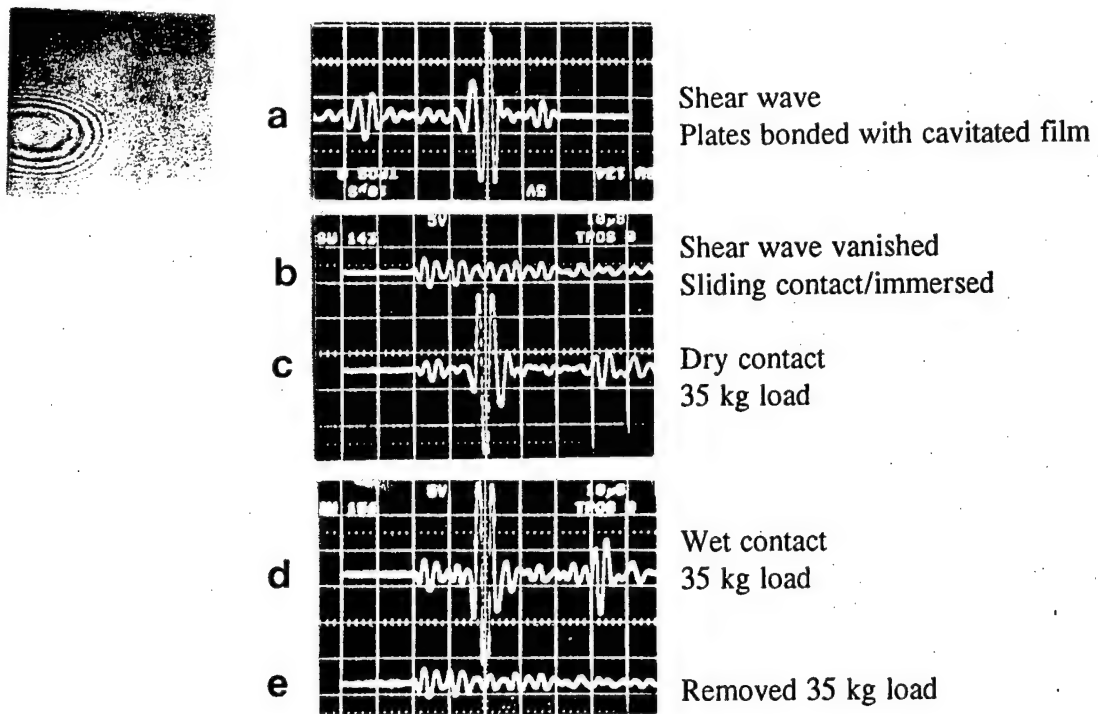


Fig. 31. Detected waveforms from two glass plate model.

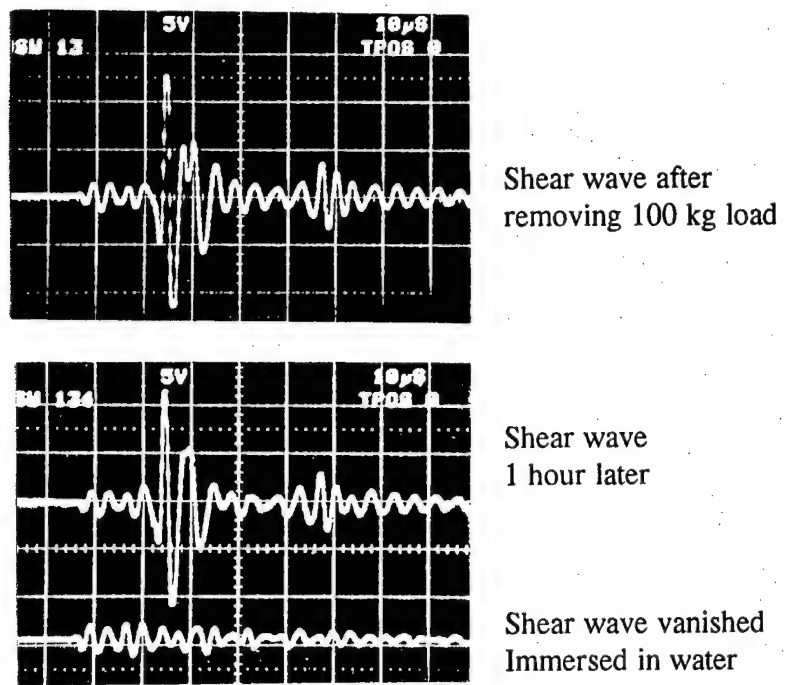


Fig. 32. Shear wave coupling between the plates continued after removing a 100 kg load.

V. CAPILLARY PHENOMENA IN GASSY SEDIMENTS

It has been known that the presence of free gas in marine sediments changes the compressional wave velocity [88] and increases the attenuation and reflectivity. Anderson and Hampton [36] used an air sac in water-saturated sediment to study the effect of gas bubbles, and modeled the scattering mechanisms as bubbles in a lossy fluid using the resonant frequency of the bubble. Fonesca et al.[82] followed Anderson and Hampton's model assuming no rigidity. Recently, Johnson, Gardiner, and Boudreau [37, 38] observed flattened vertical disc-shaped methane bubbles in marine sediments caused by fracture following linear elastic fracture mechanisms theory.

In this section, preliminary findings are described obtained from three basic experiments on capillary phenomena in gassy sediments. Air was injected through a fine metal tube in water-saturated sand. In the first experiment, the water level was flush with the sand surface (Fig. 33). In the second experiment, the sand was under a very thick water layer (Fig. 34). In the third experiment, water-saturated sand was confined in a sealed Plexiglas box (Fig. 35). When air was injected into the wet sand, 45° oblique cracks developed in the wet sediment in the three experiments. The cracks originated from the air source location, and were perpendicular to each other as shown.

In the first experiment, the sand was placed in a 4.2 cm diameter cylindrical plastic container. A fine metal tube was buried in the wet sand to inject air. The tube opening is shown in Fig. 33 (a) indicated by the white triangle. After injecting air into the saturated sand, the sand became rigid and unsaturated as 45° oblique cracks developed. When the amount of injected air was increased, the cracks opened up more and a large clump of sand was lifted forming a right-angle triangle with the sand top surface as its hypotenuse (Fig. 33(a)). The position of the lifted sand remained unchanged supported by capillary forces even after stopping the air flow (Fig. 33(d)). The fractures that resulted from the air lifting the sand formed a "scab" resembling the effect of a reflected tension shock wave pulse from a free surface of a solid as described by Kolsky [83], where the fractures started at a certain depth from the free surface.

The underwater sand from the second experiment also developed localized oblique cracks (Fig. 34(b)), however, as the amount of injected air was increased beyond a certain level, water flowed down along the cracks liquefying the sand causing partial collapse of the major air cavity (Fig. 34(c)). Several smaller air bubbles became trapped in the now locally unsaturated sand.

In the third experiment, fine water-saturated sand was sealed in a Plexiglas box (1.3 x 3.5 x 5.5 cm). A 1 mm diameter steel tube was inserted and epoxied to the box wall to inject the air into the sealed container. The white arrow in the photograph (Fig. 35(a)) points the location of the tube opening seen through the transparent Plexiglas wall before injecting the air. The sand became locally unsaturated and rigid as 45° angled cracks formed shown in Fig. 35 (b)(c) and(d). Similar to the previous example, the cracks opened up more when the air pressure was increased, and the water flowed down the

cracks liquefying the sand causing the air cavity to collapse. By continuing the injection of air, new oblique cracks formed and a second liquefaction process repeated, followed by the collapse of the newly formed air pockets. Hysteresis in the wetting and draining cycle played a role in the trapping of air bubbles and the preservation of unhealed cracks.

The seismoacoustic properties of gassy sediments are time-dependent and it is not adequate to represent the sediment as a fluid for large air pockets. It is clear from the experimental results presented here that the added stiffness and capillary forces in the localized unsaturated sand regions near the cracks increased the sediment rigidity and the compressional wave velocity. The air pockets were not spherical and their resonant frequency could not be predicted from a simple spherical bubble model.

Gardner and Sills [84] stated:

"...the Anderson and Hampton equations accurately predicted sound speed at lower frequencies of bubbles resonance and below, but results were sensitive to inappropriate values of the elastic and damping properties of the soil. The bounds of sound speed based on the elastic properties of models that simulate "compressible fluid" of "suspension" behavior were grossly misleading when applied to large bubble soils."

The presence of gas in marine sediments causes localized capillary phenomena affecting acoustic wave propagation over a wide frequency range. The air cavity is held not only by the air pressure but also by capillary forces and grain interlocking. Drained sand always retain air bubbles when rewetted. Therefore bubbles in sediment are present even when the major bubble collapses. Further research is needed to characterize the seismoacoustic properties of gassy marine sediments and develop comprehensive physical understanding of the underlying mechanisms. The aim it to come up with a realistic physical model valid for all angle of incidence and frequencies.

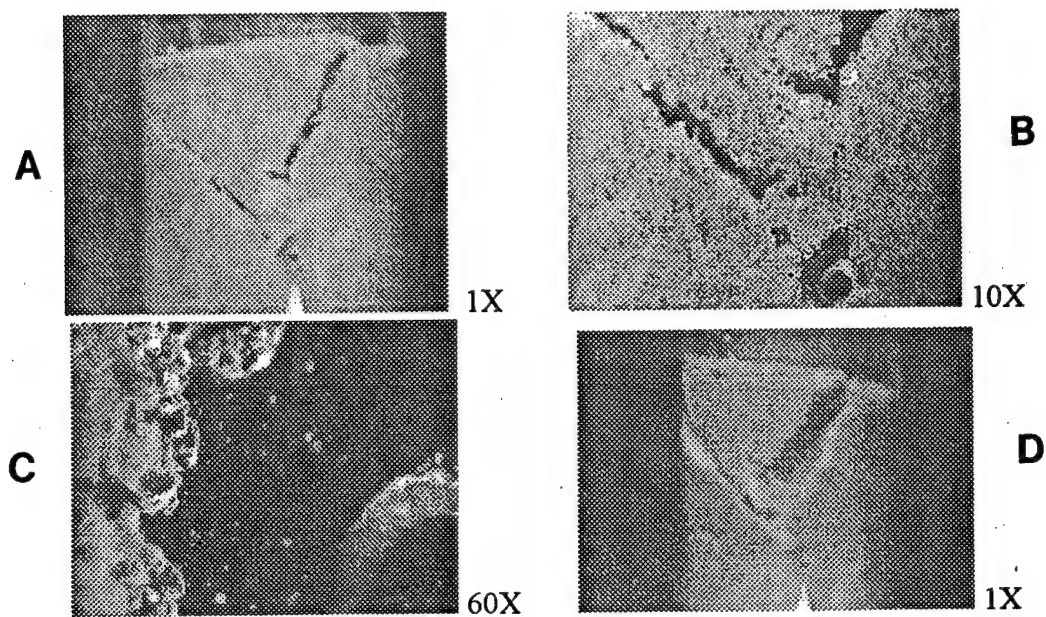


Fig. 33. Photographs from first experiment. Water level initially flush with the saturated sand surface. 45° oblique cracks developed as air was injected through the tube opening indicated by the white triangle in "A". Introducing more air increased the crack width and lifted the sand clump further "D". The expanding sand absorbed all the excess water and became unsaturated without draining any water. Capillary forces were holding the cracked sand after removing the air pressure. An expanded view near the tube opening is shown in "C".

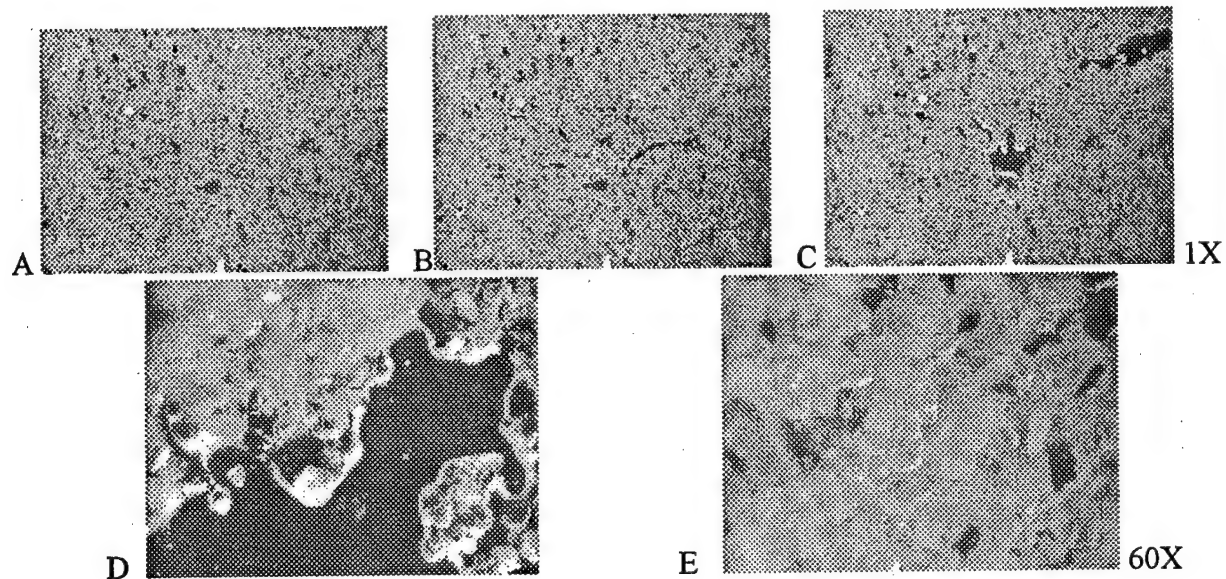


Fig. 34. Underwater sand with the tube opening buried 2.3 cm below the water/sand interface. Photograph "A" shows the tube opening and the wet sand before injecting the air. Oblique cracks developed, grew and then partially collapsed after localized liquefaction ("E").

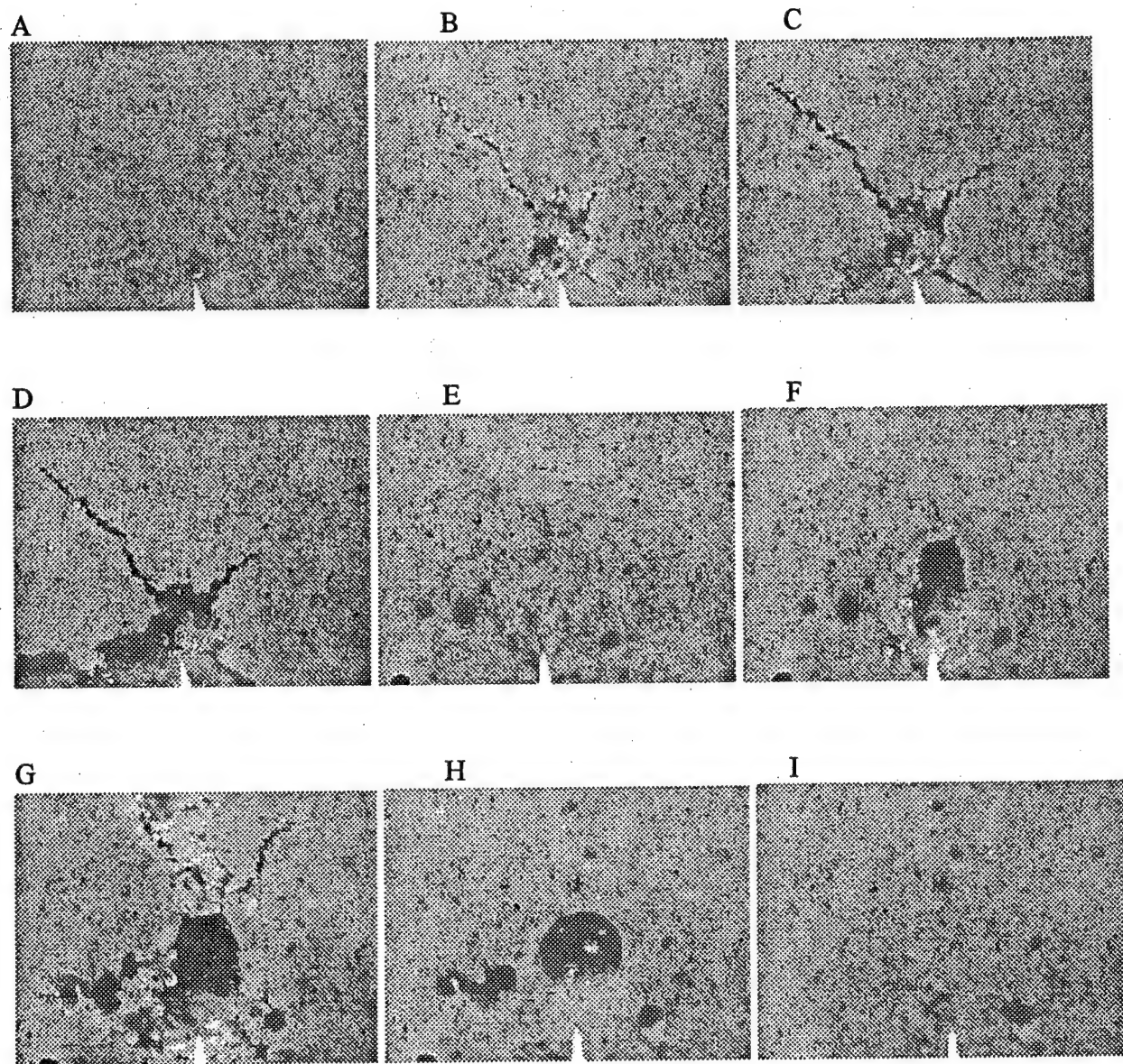


Fig. 35. Photographs from the third experiment. Seawater-saturated fine sand (Narragansett Beach, RI) placed in a sealed Plexiglas box (1.3x 3.5x 5.5 cm). A 1mm diameter steel tube was placed to inject air in the wet sand. Observed repeated formation of large 45° oblique cracks originating from the air source location followed by liquefaction and collapse of main air pocket.

VI. CONCLUSIONS

Basic experimental studies were conducted under controlled laboratory conditions revealed findings not explained by existing theories in several areas as explained below. The goal of the research is to develop fundamental understanding of high-frequency seismoacoustic phenomena to predict the penetration and attenuation of high-frequency acoustic waves interacting with the seafloor under various conditions.

Precision measurements of the high-frequency compressional wave velocity C_p in coarse water-saturated sand demonstrated that C_p decreased by 14% as frequency increased from 80-880 kHz, while the Biot theory [25] predicted an increase of about 1%. The observed dispersion characteristic is not also explained by the Buckingham theory [12, 20, 32]. The measured dispersion was 3.6% in fine saturated sand, and 3% in glass beads. The author independently confirmed the dispersion behavior reported by Guillon et al. [35] and replotted 1995 field data by Chotiros [22] from Kings Bay Experiment indicating C_p decreased by 6% as frequency increased from 5 to 60 kHz.

Two other surprising findings were observed in drained sand and glass beads. First, the author observed that the high-frequency dispersion trend in *drained* sand and glass beads was almost identical to the controversial dispersion measured in saturated sand. Second, the compressional wave velocity increased slightly when the sand was drained (and sponge dried) in contrast with the Biot-Gassman theory which predicts that the low-frequency compressional wave velocity decreases by 85% when the water content is decreased by only 1% from saturation [24].

Preliminary studies from three experiments on capillary phenomena in gassy sediments showed the formation of 45° oblique fracture cracks in water-saturated sand as air was injected. The cracks were perpendicular to each other originating from the air source location. The saturated sand became locally unsaturated and rigid due to capillary forces. The findings clearly indicated the limitation of the Anderson and Hampton's model [36] representing the gassy sediment as a fluid. Further research is needed to explain the observed 45° oblique fracture cracks that differ considerably from the flattened vertical disc-shaped methane bubbles caused by fracture in marine sediments recently reported by Johnson, Gardiner, and Boudreau [37, 38].

In order to better understand grain to grain shear coupling, the author measured shear wave coupling and visualized seawater capillary mechanisms between two microglass plates revealing complex hidden phenomena on solid-like behavior of confined seawater film, capillary cavitation, water trapping, confined salt crystallization, dendritic formation, air entrainment, tapered capillary desalination, and loading hysteresis.

Further research is needed in several areas to better understand and characterize the high-frequency seismoacoustic properties of marine sediments under various conditions important for reliable detection and imaging of buried objects.

VII. REFERENCES

1. R. D. Stoll, "Comments on "Biot model of sound propagation in water-saturated sand," [J. Acoust. Soc. Am. 97, 199-214 (1995)]," J. Acoust. Soc. Am. 103 (5), 2723-2725 (1998).
2. E. I. Thorsos, D. R. Jackson, and K. L. Williams, "Modeling of subcritical penetration into sediments due to interface roughness," J. Acoust. Soc. Am. 107, 263-277 (2000).
3. H. J. Simpson, B. H. Houston, L. S. Couchman, "Measurement and modeling of sound propagation into unconsolidated water-saturated porous media in a laboratory," J. Acoust. Soc. Am. 104(3), Pt. 2, 1787 (1998).
4. F. A. Boyle and N. P. Chotiros, "Experimental detection of a slow acoustic wave in sediment at shallow grazing angles," J. Acoust. Soc. Am. 91, 2615-2619 (1992).
5. N. P. Chotiros, "An inversion for Biot Parameters in water-saturated sand," J. Acoust. Soc. Am. 112(5) 1853-1868 (2002).
6. K. L. Williams, "An effective density fluid model for acoustic propagation in sediments derived from Biot theory," J. Acoust. Soc. Am. 110(5), 2276-2281 (2001).
7. C. J. Hickey and J. M. Sabatier, "Choosing Biot parameters for modeling water-saturated sand," J. Acoust. Soc. Am. 102(3) 1480-1484 (1997).
8. K. Briggs, "Empirical relationships among sediment properties and acoustic properties for the continental shelf seafloor," J. Acoust. Soc. Am. 111(5) 2333 (2002).
9. K. L. Williams, D. R. Jackson, E. I. Thorsos, D. Tang, and S. G. Schock, "Comparison of sound speed and attenuation measured in a sandy sediment to predictions based on the Biot theory of porous media," IEEE, J. Ocean. Eng. 27(3) 413-428 (2002).
10. J. R. Chamuel, "An explanation for the anomalous ultrasonic slow wave in underwater sand," IEEE Trans. Ultrasonics and Freq. Control, 45(6), 1441-1443 (1998).
11. A. Maguer, W. L. J. Fox, H. Schmidt, E. Pouliquen and E. Bovio, "Mechanisms for subcritical penetration into a sandy bottom: Experiments and modeling results," J. Acoust. Soc. Am. 107, 1215-1225 (2000).
12. M. J. Buckingham, "Theory of compressional and shear waves in fluidlike marine sediments," J. Acoust. Soc. Am. 103, 288-299 (1998).
13. M. J. Buckingham, "Theory of acoustic attenuation, dispersion, and pulse propagation in unconsolidated granular materials including marine sediments," J. Acoust. Soc. Am. 102(5) 2579-2596 (1997).
14. Y. Mu, M. Badiey, and A. H.D. Cheng, "Parameter uncertainty analysis on acoustic response in fluid filled poroelastic media," J. Acoust. Soc. Am. 106(1) 151-163 (1999).
15. E. I. Thorsos, K. L. Williams, D. R. Jackson, D. Tang, K. B. Briggs, "Extending the legacy of Ed Hamilton in high-frequency sediment acoustics," J. Acoust. Soc. Am. 111(5), 2329 (2002).
16. E. I. Thorsos, K. L. Williams, N. P. Chotiros, J. T. Christoff, K. W. Commander, C. F. Greenlaw, D. V. Holliday, D. R. Jackson, J. L. Lopes, D. E. McGehee, M. D. Richardson, J. E. Piper, and D. Tang, "An overview of SAX 99: Acoustic measurements," IEEE J. Ocean Eng. 26, 4-25 (2001).
17. H. J. Simpson, B. H. Houston, S. W. Liskey, P. A. Frank, A. R. Berdoz, L. A. Kraus, C. K. Frederickson, and S. Stanic, "At sea measurements of sound penetration into sediments using a buried vertical synthetic array," J. Acoust. Soc. Am. 114(3), 1281-1290 (2003).
18. M. D. Richardson, "Shear waves in surficial sediments: Revisited," J. Acoust. Soc. Am. 111(5), 2333 (2002).
19. N. P. Chotiros and M. J. Isakson, "A broadband ocean sediment acoustics model for signal processing applications," J. Acoust. Soc. Am. 112(5) 2310 (2002).
20. M. J. Buckingham, "Wave propagation, stress relaxation, and grain-to-grain shearing in saturated, unconsolidated marine sediments," J. Acoust. Soc. Am. 108(6) 2796-2815 (2000).
21. J. R. Chamuel, *Effect of Water Content and Sea Salt on Seismoacoustic Waves in Beach Sand*, Sonoquest Advanced Ultrasonics Research, Wellesley Hills, Massachusetts, Report No. JRC-42-2001, September 2001 (NTIS Document Accession No. AD-A395391).
22. N. P. Chotiros, "Biot model of sound propagation in water-saturated sand," J. Acoust. Soc. Am. 97(1) 199-214 (1995).

23. N. P. Chotiros, "Response to: 'Comments on Biot model of sound propagation in water-saturated sand,'" *J. Acoust. Soc. Am.* 103(5), Pt. 1, 2726-2729 (1998).

24. R. Bachrach and A. Nur, "High-resolution shallow-seismic experiments in sand, Parts I and II," *Geophysics* 63(4), 1225-1233, 1234-1240 (1998).

25. M. A. Biot, "Theory of propagation of elastic waves in a fluid-saturated porous solid. II : Higher-frequency range," *J. Acoust. Soc. Am.* 28, 179-191 (1956).

26. D. J. Wingham, "The dispersion of sound in sediment," *J. Acoust. Soc. Am.* 78(5) 1757-1760 (1985).

27. A. Turgut and T. Yamamoto, "Measurements of acoustic wave velocities and attenuation in marine sediments," *J. Acoust. Soc. Am.* 87 (6), 2376-2383 (1990).

28. T. Yamamoto, "Imaging the permeability structure within the near-surface sediments by acoustic crosswell tomography," *J. Appl. Geophys.* 47, 1-10 (2001).

29. A. Turgut, "An investigation of causality for Biot models by using Kramers-Kronig relations," *Shear Waves in Marine Sediments*, edited by J. M. Hovem, M. D. Richardson, and R. D. Stoll, Kluwer Academic Pub., Netherlands, pp 21-28, 1991.

30. R. D. Stoll, *Sediment Acoustics*, Vol. 26, (Springer-Verlag, Berlin, 1989).

31. M. A. Biot, "Theory of propagation of elastic waves in a fluid-saturated porous solid, Part I: Low frequency range," *J. Acoust. Soc. Am.* 28, 168-178 (1956).

32. M. J. Buckingham, "Theory of acoustic attenuation, dispersion, and pulse propagation in unconsolidated granular materials including marine sediments," *J. Acoust. Soc. Am.* 102 (5), 2579-2596 (1997).

33. R. P. Gilbert and A. Pachenko, "Effective acoustic equations for a two-phase medium with microstructure," *SIAM Conference on Mathematical and Computational Issues in the Geosciences (GS03)*, March 17-20, 2003, Austin, (2003).

34. J. R. Chamuel, "New Controversial Inverse Dispersion of High-Frequency Compressional Waves in Saturated Sediments," Sonoquest Advanced Ultrasonics Research., Wellesley Hills, Massachusetts, Document No. JRC-16-03, Brief Communication 4 Sept. 2003.

35. L. Guillou, A. Moussatov, B. Brouard, and C. Ayrault, "Propagation of sound in sands: Measurements and modeling," *Oceans '98*, 380-384 (1998).

36. A. L. Anderson and L. D. Hampton, "Acoustics of gas-bearing sediments. II. Measurements and models," *J. Acoust. Soc. Am.* 67(6) 1890-1903 (1980).

37. B. P. Boudreau, B. Gardiner, and B. Johnson, "Rate of growth of isolated bubbles in sediments with a distributed diagenetic source of methane," *Limnology and Oceanography* 46, 616-622 (2001).

38. B. S. Gardiner, B. P. Boudreau, and B. D. Johnson, "Growth of disc-shaped bubbles in sediments," *Geochimica et Cosmochimica Acta* 67(8) 1485-1494 (2003).

39. J. R. Chamuel, "Seismoacoustic Waves in Water-Covered Sand," Sonoquest Advanced Ultrasonics Research., Wellesley Hills, Massachusetts, Report No. JRC-74-99, 1999. (NTIS # AD-A373739).

40. J. R. Chamuel, "Ultrasonic studies on the effect of water content on compressional wave velocity in beach sand," *J. Acoust. Soc. Am.* 108(5), Pt. 2, Paper 2pUW11, 2536 (2000).

41. J. R. Chamuel, "Effect of seawater salt on compressional wave in dry beach sand," *J. Acoust. Soc. Am.* 109(5), Pt. 2, Paper 5aUW10, 2496 (2001).

42. A. P. Koesoemadinata and G. A. McMechan, "Empirical estimation of viscoelastic seismic parameters from petrophysical properties of sandstone," *Geophysics* 66, 1467-1470 (2001).

43. D. Velea, *The Effect of Moisture on the Propagation of Compressional and Shear Waves in Ottawa Sand*, Ph.D. Thesis, The University of Mississippi, May 1998.

44. H. M. Tavossi and B. R. Tittman, "Acoustic signal attenuation, velocity, and filtering by beach sand, with different water content," *J. Acoust. Soc. Am.* 105(2), 1385 (1999).

45. F. D. Shields, J. M. Sabatier, and M. Wang, "The effect of moisture on compressional and shear wave speeds in unconsolidated granular material," *J. Acoust. Soc. Am.* 108 (5), 1998-2004 (2000).

46. C. Gay and L. Leibler, "Theory of tackiness," *Physical Review Letters* 82(5), 936-939 (1999).

47. C. Creton, J. C. Hooker, and K. R. Shull, "Bulk and interfacial contributions to the debonding mechanisms of soft adhesives," *Langmuir* 17, 4948-4954 (2001).

48. C. M. Aracne-Ruddle, B. P. Bonner, C. N. Trombino, E. D. Hardy, P. A. Berge, C. O. Boro, D. Wildenschild, C. D. Rowe, and D. J. Hart, "Ultrasonic velocities in unconsolidated sand/clay mixtures at low pressures," American Geophysical Union Fall Meeting, San Francisco, CA Dec 13-17 (1999). Lawrence Livermore National Lab. Preprint # UCRL-JC-135621.

49. P. G. Howe, D. P. Benton, and I. E. Puddington, "London-van der Waals attractive forces between glass surfaces," Canadian J. Chemistry 33, 1375-1383 (1955).

50. A. W. Adamson, *Physical Chemistry of Surfaces*, Interscience Publisher (1967).

51. J. S. McFarlane and D. Tabor, "Adhesion of solids and the effect of surface films," Proc. Royal Soc. London A 202, 224-243 (1950).

52. M. J. Mathewson and H. J. Mamin, "Liquid mediated adhesion of ultra-flat solid surfaces," Materials Research Society Symposium Proceedings Vol. 119, *Adhesion in Solids*, Editors D. M. Mattox, J. E. Baglim, R. J. Gottschall, and C. D. Batick, Pittsburgh, PA (1988).

53. W. J. Likos and N. Lu, "Hysteresis of capillary cohesion in unsaturated soils," 15th ASCE Eng. Mech. Conf. June 2-5, 2002, Columbia University, New York (2002).

54. V. D. Sobolev, N. V. Churaev, M. G. Verlade, and Z. M. Zorin, "Surface tension and dynamic contact angle of water in thin quartz capillaries," J. Colloid Interface Sci. 222, 51-54 (2000).

55. C. M. Megaridis, A. Güvenç Yazicioglu, J. A. Libera, and Y. Gogotsi, "Attoliter fluid experiments in individual closed-end carbon nanotubes: Liquid film and fluid interface dynamics," Physics of Fluids 14(2) L5-L8 (2002).

56. F. van der Veen, M. Zwanenburg and W. J. Huisman, "Layering at the solid-liquid Interface," Syncrotron Radiation News 12(2), 47 (1999).

57. J. Stefan, "Versuche über die Scheinbare Adhesion," Math. Naturwissenschaftliche Klasse, Wien. Sitzungs-herichte 69, 713 (1874).

58. F. R. Eirich and Tabor, Proc. Cambridge Phil. Soc. 44, 566 (1948).

59. L. A. Archer, D. Ternet, and R. G. Larson, "Fracture phenomena in shearing flow in viscous liquids," Rheology Acta 36, 579-584 (1997).

60. R. Evans, "Fluids adsorbed in narrow pores: phase equilibria and structure," J. Phys.: Condens. Matter 2, 8989-9007 (1990).

61. Nobuo Maeda, *Phase Transitions of Long-Chain N-Alkanes at Interfaces*, PhD thesis, Department of Applied Mathematics, The Australian National University, January (2001).

62. L. Briggs, "Limiting negative pressure of water," J. Appl. Phys. 21, 721-722 (1950).

63. D. Or and M. Tuller, "Cavitation during desaturation of porous media under tension," Water Resources Research 38(5), 19.1-19.4(2002).

64. R. S. Chahal and R. N. Yong, "Validity of the soil water characteristics determined with the pressure apparatus," Soil Sci 99, 98-103 (1965).

65. I. Chikina and C. Gay, "Cavitation in adhesives," Physical Review Letters 85(21) 4546-4549 (2000).

66. P. R. Williams and M. S. Barrow, "Using a modified atomic microscope to study meso-scale cavitation in stretched liquid films," NATO ARW Liquids Under Negative Pressure, Feb. 23-25, Budapest, Hungary (2002).

67. M. Smith and D. R. Vrane, "Deformation and rupture in confined, thin liquid films driven by thermocapillarity," Chapter 17, *Fluid Dynamics at Interfaces*, edited by W. Shyy and R. Narayanan, Cambridge University Press (2002).

68. Y.L. Chen and J. Israelachvili, "New mechanism of cavitation damage," Science 252, 1157-1160 (1991).

69. T. Kuhl, M. Ruths, Y. L. Chen, and J. Israelachvili, "Direct visualization of cavitation damage in ultrathin liquid films," J. Heart Valve Disease 3(1) 117-127 (1994).

70. N. Y. Denisov and B. F. Reltov, "The influence of certain processes on the strength of soils," Proc. of the Fifth Int. Conf. on Soil Mechanics and Foundation Eng., Paris 75-78 (1961).

71. J. K. Mitchell and Z. V. Solymer, "Time dependent strength gain in freshly deposited or densified sand," J. Geotech. Eng. 110(11), 1559-1576 (1984).

72. W. Losert, J. C. Geminard, S. Nasuno, and J. P. Gollub, "Mechanisms for slow strengthening in granular materials," Physical Review E 61(4), 4060-4068 (2000).

73. M. E. Zolensky, R. J. Bodnar, E. K. Gibson, L. E. Nyquist, Y. Reese, Chi-Yu Shih, and H. Wiesmann, "Asteroidal water within fluid inclusion-bearing halite in an H5 chondrite, Monahans (1998)," *Science*, 285, 1377-1379 (1999).

74. F. Renard and P. Ortoleva, "Water films at grain-grain contacts: Debye-Hückel, osmotic model of stress, salinity and mineralogy dependence," *Geochimica et Cosmochimica Acta* 61, 1963-1970 (1997).

75. R. D. Deegan, O. Bakajin, T. F. Dupont, G. Huber, S. R. Nagel, and T. Witten, "Capillary flow as the cause of ring stains from dried liquid drops," *Nature* 389, 827-830 (1997).

76. L. Shmuylovich, A. Q. Shen, and H. A. Stone, "Surface morphology of drying latex films: Multiple ring formation," *Langmuir* (2002).

77. H. Bouasse, *Capillarité Phénomènes Superficiels*, Delagrave, Paris (1924).

78. B. N. J. Persson, F. Bucher, and B. Chiaia, "Elastic contact between randomly rough surfaces: Comparison of theory with numerical results," *Physical Review B* 65, 184106 1-7 (2002).

79. A. W. Bush, R. D. Gibson, and T. R. Thomas, "The elastic contact of a rough surface," *Wear* 35, 87-111 (1975).

80. T. Halsey and A. Levine, "How sandcastles fall," *Phys. Rev. Lett.* 80, 3141 (1998).

81. V. N. Belomestnych and E. M. Karpova, "Acoustic and elastic properties models Ionik and ion-molecular crystals," XI Session of the Russian Acoustical Society, Moscow, Nov. 19-23 (2001).

82. L. Fonseca, L. Mayer, D. Orange, and N. Driscoll, "The high-frequency backscattering angular response of gassy sediments: Model/data comparison from the Eel River Margin, California," *J. Acoust. Soc. Am.* 111(6) 2621-2631 (2002).

83. H. Kolsky, *Stress Waves in Solids*, Dover Publications, New York Fig. 44, page 187 (1963).

84. T. N. Gardner and G. C. Sills, "An examination of the parameters that govern the acoustic behavior of seabed sediments containing gas bubbles," *J. Acoust. Soc. Am.* 110(4), 1878-1889 (2001).

85. E. L. Hamilton, "Compressional wave attenuation in marine sediments," *Geophysics* 37(4) 620-646 (1972).

86. H. E. Anderson, "Vicinal, long-range and extremely long range effects on growth of sodium chloride crystals from aqueous solutions containing protein," *Appl. Physics Comm.* 4(2-3), 217-239 (1984).

87. F. Gassman, "Über die Elastizität poröser Medien," *Vierteljahrsschrift der Naturforschenden Gesellschaft* 96, 1-23 (1951).

88. T. N. Gardner, "An acoustic study of soils that model seabed sediments containing gas bubbles," *J. Acoust. Soc. Am.* 107(1) 163-176 (2000).

89. M. Jacoby, J. Dvorkin, and X. Liu, "Elasticity of partially saturated frozen sand," *Geophysics* 61(1), 288-293 (1996).